

# Ammonia Catalyst Evolution Under Reactor Conditions Revealed by Environmental and Multimodal Electron Microscopy

Amy S. McKeown-Green<sup>1†\*</sup>, Parivash Moradifar<sup>2†\*</sup>, Zisheng Zhang<sup>3,4</sup>, Cedric Lim<sup>2</sup>, Andrew Barnum<sup>5</sup>, Lin Yuan<sup>2</sup>, Robert Sinclair<sup>2</sup>, Frank Abild-Pedersen<sup>4</sup>, Colin Ophus<sup>2</sup>, Jennifer A. Dionne<sup>2\*</sup>.

Affiliations:

<sup>1</sup> Chemistry Department, Stanford University, Stanford, CA, USA.

<sup>2</sup> Materials Science and Engineering Department, Stanford University, Stanford, CA, USA.

<sup>3</sup> Department of Chemical Engineering, Stanford University, Stanford, CA, USA

<sup>4</sup>SUNCAT Center for Interface Science and Catalysis, SLAC National Accelerator Laboratory, Menlo Park, CA, USA

<sup>5</sup>Stanford Nano Shared Facilities, Stanford University, Stanford, CA, USA

<sup>†</sup>These authors contributed equally to this work

\*Corresponding authors. Email: [amygreen@stanford.edu](mailto:amygreen@stanford.edu); [pmoradi@stanford.edu](mailto:pmoradi@stanford.edu); [jdionne@stanford.edu](mailto:jdionne@stanford.edu)

## Abstract

Bimetallic catalysts provide new routes toward sustainable ammonia synthesis, but the structural dynamics controlling their performance under real-world conditions remain poorly understood. Here, we combine *in situ* gas-cell and multimodal electron microscopy to disentangle the temperature-, pressure-, and chemistry-dependent restructuring of AuRu catalysts, revealing pathways accessible only at atmospheric pressure. As synthesized, AuRu nanocatalysts are polycrystalline face-centered-cubic alloys with Au/Ru intermixing that phase-segregate into Au- and Ru-rich domains with elevated temperature ( $>450$  °C). Increased pressure (~1 atm in 3:1, hydrogen:nitrogen) unlocks pronounced faceting and internal nanovoid formation, which systematic gas-chemistry variation identifies as hydrogen-driven. Density functional theory-based interatomic potentials show that hydrogen can amplify Au/Ru diffusion asymmetry, promoting nanovoid formation via a gas-mediated Kirkendall mechanism. Together, these results bridge the pressure gap between traditional *in situ* electron microscopy and benchtop ammonia reactors, enabling resolution of distinct restructuring stimuli in multicomponent systems.

## Bridging the pressure gap in ammonia catalysis reveals new restructuring pathways

Ammonia ( $\text{NH}_3$ ) is a cornerstone of global agriculture, serving as the primary chemical feedstock for nitrogen-based synthetic fertilizers, which underpin more than half of global food production (1). Today, most synthetic  $\text{NH}_3$  is produced via the Haber-Bosch process, a heterogeneous catalytic reaction of gaseous  $\text{N}_2$  and  $\text{H}_2$  over Ru-based and Fe-based catalysts operated at elevated temperatures (350–500°C) and extreme pressures (150–300 atm) (2). These conditions contribute to the Haber-Bosch process being highly energy-intensive, consuming ~2% of global energy and producing ~1.3% of global  $\text{CO}_2$  emissions annually (3). To address these challenges, a broad suite of electrochemical (4–6), thermal (7–9), and photocatalytic (10–12) platforms has been developed to enable  $\text{NH}_3$  synthesis under milder conditions.

Delivering milder pathways, however, places strict demands on catalyst design, motivating the use of multicomponent alloys to tune  $\text{N}_2$  activation, charge transfer, and optical or thermal responses (13, 14). For example, alloys such as AuRu and CuFe couple strong N-binding metals with plasmonically active hosts, enabling  $\text{NH}_3$  synthesis under atmospheric pressure (1 atm) (15–17). Yet, these types of synergistic catalysts are structurally complex, exhibiting strain, chemical-potential variations, and compositional gradients that promote dynamic restructuring under reactive conditions (18, 19). Currently, bench-top reactors do not permit real-time monitoring of catalyst evolution at the single-particle level, limiting observations to before-and-after snapshots. Resolving these structural changes requires *in situ* characterization that directly links structural evolution to the operating conditions that drive it.

Environmental transmission electron microscopy (E-TEM) has proven to be a powerful tool for capturing nanoscale structural, optical, and chemical changes in reactive gas environments (20–26). Its application to  $\text{NH}_3$  synthesis for Ru-based catalysts has resolved how insulating supports stabilize catalytically active sites (27, 28). However, traditional differential pumping of the TEM column has confined such studies to pressures of  $10^{-5}$ – $10^{-4}$  atm, leaving a pressure gap of nearly four orders of magnitude between ambient-pressure  $\text{NH}_3$  reactors and their *in situ* TEM counterparts (27, 28). As gas pressure fundamentally alters adsorption kinetics and surface diffusion (29), closing this pressure gap is essential for accessing real-world conditions and assessing pressure-dependent catalyst restructuring.

To close this gap and interrogate catalyst evolution under realistic reaction environments, we employ an *in situ* gas-cell scanning transmission electron microscopy (STEM) platform (Fig. 1A) that supports reactive  $\text{H}_2:\text{N}_2$  gas mixtures up to 1 atm. We focus on AuRu alloys as a representative bimetallic catalyst for atmospheric-pressure  $\text{NH}_3$  synthesis, providing a platform for real-time visualization of restructuring under reactor-relevant conditions. As *in situ* STEM imaging alone is mainly limited to  $Z$  (atomic number)-contrast, resolving these transformations requires correlative measurements that connect optical, structural, and morphological information.

We therefore combine atomic-resolution imaging with electron spectroscopy, diffraction, and tomography in a multimodal framework that maps changes across individual particles. The resulting multidimensional datasets link nanoscale evolution across structure and chemistry, revealing restructuring pathways that *in situ* imaging alone cannot access.

Using multimodal electron microscopy, we systematically decouple the effects of temperature, pressure, and gas chemistry on AuRu catalysts. Pristine AuRu (1:0.2) nanocatalysts exhibit a polycrystalline FCC structure with Au–Ru intermixing. Vacuum annealing isolates a thermally driven restructuring pathway in which temperatures above 450 °C drive Au–Ru phase segregation into discrete Au (FCC) and Ru (HCP) domains. Building on this temperature-dependent restructuring, we introduce H<sub>2</sub>:N<sub>2</sub> (3:1) at increasing pressures to probe restructuring under NH<sub>3</sub>-relevant conditions. At atmospheric pressure, the nanocatalysts develop sharpened facets and, in some cases, internal nanovoids, revealing pressure-driven restructuring which is absent under vacuum. Systematic variation of the gas chemistry (Ar, N<sub>2</sub>, H<sub>2</sub>) shows that pure Ar and N<sub>2</sub> reproduce vacuum restructuring, whereas pure H<sub>2</sub> uniquely induces nanovoid formation, identifying hydrogen as the key chemical driver. DFT-trained machine-learning interatomic potentials (MLIP) used to calculate relative Au/Ru diffusion barriers support a hydrogen-driven Kirkendall effect, whereby absorbed H atoms alter Au–Ru interdiffusion to drive vacancy clustering into nanovoids. Collectively, these correlative *in situ*, multidimensional, and multimodal measurements close the pressure gap in electron-microscopy studies of NH<sub>3</sub> synthesis and establish a general framework for resolving coupled temperature, pressure, and chemical driving forces in multicomponent systems.

## **Increased temperature drives phase segregation in AuRu nanocatalysts**

In their pristine state, the AuRu nanocatalysts are polycrystalline and frequently pentatwinned with an FCC lattice (Fig. 1B). Atomic high-angle annular dark field (HAADF)-STEM reveals a lattice constant of 0.405 nm, which is slightly lower than that of pure Au (0.408 nm) and consistent with Ru-alloying (Fig. 1B inset). AuRu intermixing is found to persist at the single particle level despite bulk-phase immiscibility (30, 31); this is confirmed by X-EDS elemental maps, which show an even spatial distribution of characteristic Au La/M $\alpha$  and Ru Ka/L $\alpha$  peaks (Fig. 1C, Fig. S1). Quantitative X-EDS analysis shows an Au:Ru ratio of 1:0.16 (Table S1). Monochromated low-loss electron energy loss spectroscopy (EELS) reveals a persistent Au plasmon appearing near 2.5 eV (Fig. 1D), consistent with Ru alloying (17). 4D-STEM dark-field imaging, coupled with single-point nanobeam electron diffraction patterns, highlights the structural polydispersity across the ensemble, illuminating diverse internal grain structures and orientations consistent with the particles’ FCC crystal structure (Fm-3m) (Fig. 1E, F). The structural diversity likely reflects alloying-induced strain, which facilitates the formation of stacking faults and twin boundaries (32). Additional HAADF-STEM characterization reveals a

particle-size distribution with a mean diameter of  $25 \pm 6$  nm (Fig. S2), indicating relative size uniformity despite structural heterogeneity.

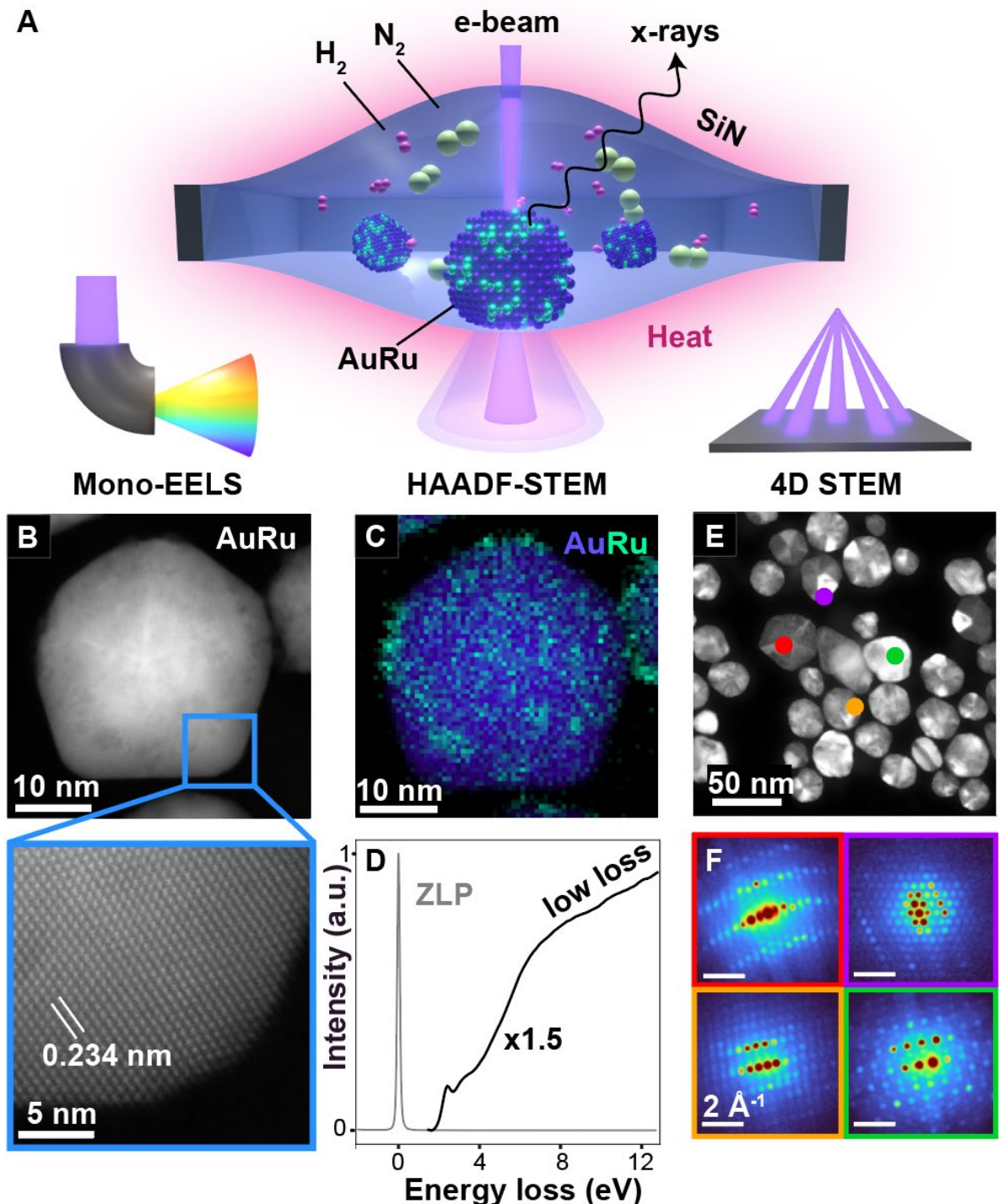


**Fig. 1. Multi-modal characterization of pristine AuRu nanocatalysts prior to thermal annealing or gas-phase catalysis.** (A) Schematic of the experimental setup showing the high-pressure gas-cell integrated

with HAADF-STEM, along with monochromated EEL and 4D-STEM modalities used post-reaction. **(B)** Atomic-resolution HAADF-STEM image of a representative polycrystalline AuRu (1:0.2) bimetallic nanocatalyst with an inset showing atomic columns and measured lattice constant. **(C)** X-EDS elemental map of the particle in (B) shows intermixing of Au and Ru via the characteristic Au La/M $\alpha$  and Ru Ka/L $\alpha$  peaks. Particle linescans are shown in Fig. S1. **(D)** Overlaid monochromated dual-EELS spectrum showing the separate zero-loss peak (ZLP) and low-loss region with the AuRu plasmon resonance near 2.5 eV. **(E)** 4D-STEM dark-field image of pristine AuRu nanocatalysts revealing internal grain structure; full orientation maps are shown in Fig. S3. **(F)** Representative diffraction patterns from individual probe positions in (E), confirming FCC crystal structure (Fm-3m space group). Orientation assignment can be found in Fig. S3. **(B-F)** Data has been acquired under vacuum on a standard SiN window.

Having established the as-synthesized morphology, composition, and crystal structure of the AuRu catalysts, we next isolate how temperature drives restructuring by annealing the samples under vacuum. Under these conditions, Au–Ru dealloying and phase transition are observed, yielding distinct Ru-rich and Au-rich regions with different crystal structures.

To track the onset and progression of this temperature-driven restructuring, we perform a stepwise annealing protocol with a blanked electron beam, increasing the temperature at 20°C/min, with 10-min holds at 50°C intervals, briefly unblanking to image the same nanocatalysts at each step. Phase segregation typically initiates between 450 and 650°C, with the onset systematically shifting to higher temperatures for larger particles. Under HAADF-STEM imaging, emergent Ru-rich domains appear as lower-Z, dark-contrast regions that increase in size with temperature (Fig. 2A). Near-complete phase segregation is also shown by X-EDS elemental mapping (Fig. 2B), which resolves spatially distinct Au and Ru regions in contrast to the intermixed distributions observed in the as-synthesized state (Fig. 1C). We further find that particle size and intrinsic chemical heterogeneity influence the number of Ru-rich domains that form, with some particles developing two to three distinct Ru-rich regions within them during segregation.

To account for the effects of the STEM probe, we repeat the protocol in high-resolution TEM (HRTEM), where the Ru-rich domain appears lighter under bright-field parallel illumination yet exhibits the same temperature dependence, further corroborated by X-EDS (Fig. 2C, D). Additionally, as catalyst restructuring can be strongly influenced by catalyst–support interactions, we perform identical vacuum-annealing experiments on AuRu nanocatalysts supported on MgO. Phase segregation is also observed under these conditions, indicating that support interactions alone are unlikely to influence this thermally enabled restructuring (Fig. S4). Additional statistics for unsupported particles imaged by HRTEM are shown in Fig. S5.

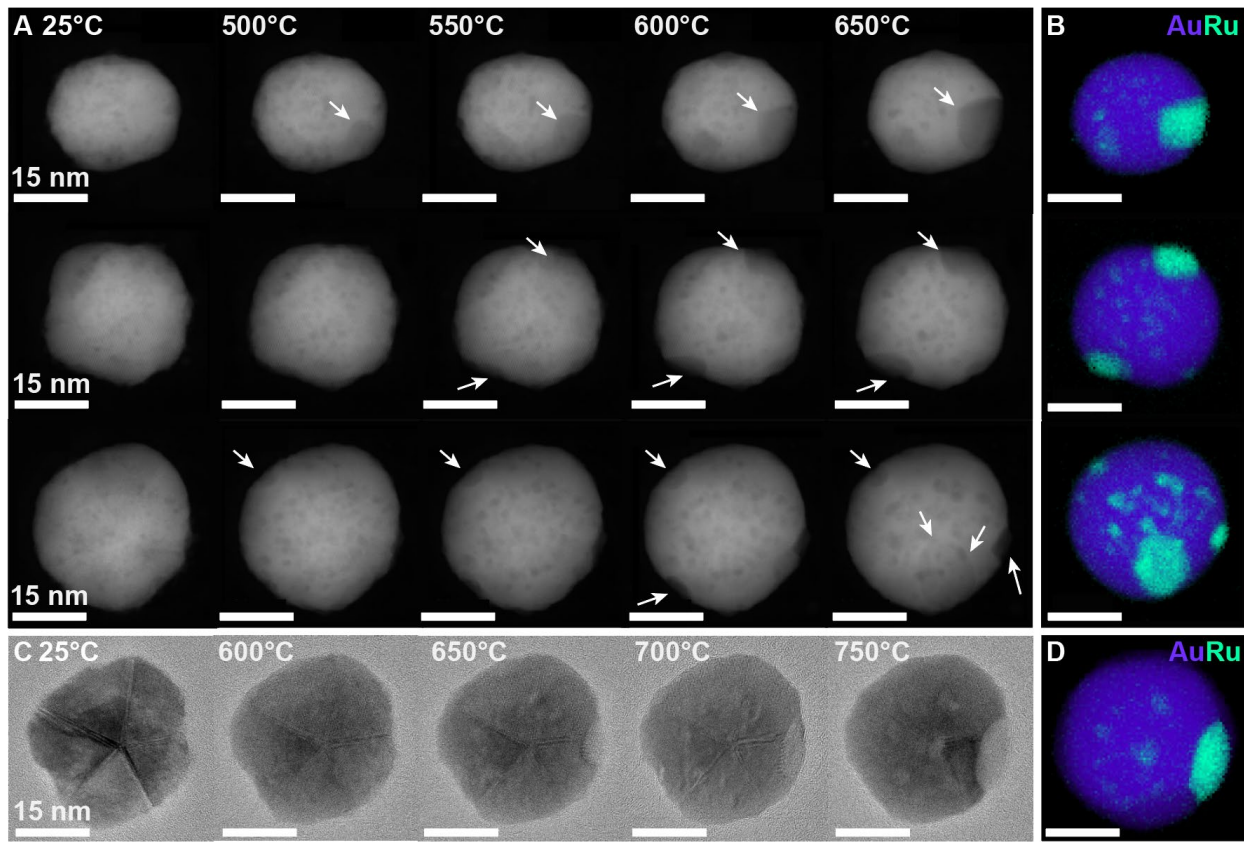


**Fig. 2. Vacuum annealing induced Au–Ru phase segregation.** (A) STEM-HAADF image series of three representative AuRu nanocrystals of increasing size during stepwise heating from room temperature (RT) to 750 °C at a 20 °C/min ramp rate with 10-min holds at each temperature. Progressive Au–Ru phase segregation is denoted by two regions of distinct Z-contrast (Au - light, Ru - dark), indicated by white arrows. (B) X-EDS elemental maps of the same three particles post-vacuum annealing, confirming spatial segregation of Au and Ru via the characteristic Au La/Ma and Ru Ka/La peaks. (C) HRTEM image series of a particle under the same heating protocol serves to eliminate the role of focused-probe in phase-segregation (Au-dark, Ru-light). (D) Corresponding X-EDS elemental map of the characteristic Au La/Ma and Ru Ka/La peaks.

Having established that temperature-driven Au–Ru phase segregation is robust to beam conditions and catalyst support, we next examine the atomic structure and crystallography of the resulting Au- and Ru-rich regions. At the Au–Ru interface, atomic-resolution HAADF-STEM reveals a classical close-packed plane orientation between the close-packed Au FCC {111} planes (0.235 nm measured) and Ru HCP {0002} planes (0.216 nm) (33, 34). This is consistent with an FCC-to-HCP phase transition of Ru during dealloying (Fig. 3A), which has been observed in related AuRu systems and reflects Ru's thermodynamic preference for the HCP structure (35).

To obtain statistically representative insight into phase segregation across the catalyst particle ensemble, we employ 4D-STEM with a patterned bullseye aperture across a sample region

containing more than 20 particles (36). The patterned aperture enhances Bragg peak discrimination against the amorphous background. Although the summed diffraction pattern is dominated by FCC reflections (Fig. 3B), analysis of the Bragg vector histogram resolves contributions from both Au FCC and Ru HCP phases (Fig. 3C). Automated crystal orientation mapping (ACOM) with FCC/HCP phase assignment yields spatial maps of distinct Au-rich and Ru-rich regions (Fig. 3D) (37). Example single-point diffraction patterns are shown in Figs. 3E-F (assignment in Figs. S6-7). Quantification indicates Ru domains with an average size of  $7 \pm 4$  nm and an overall composition of 82% Au and 18% Ru ( $\text{Au:Ru} \approx 1:0.22$ ), consistent with the nominal composition ( $\text{Au:Ru} = 1:0.2$ ) and indicating near-complete phase separation without measurable Ru loss. This diffusion and segregation of Ru, along with its FCC-HCP phase transition, may transform the coordination environment of Ru atoms, a key determinant of catalytic activity.

Beyond altering the elemental distribution, this phase segregation also reshapes the electronic and optical response of the nanocatalysts, which has previously been shown to influence catalytic activity (15, 17). Using monochromated EELS, we excite and probe the catalysts' plasmonic response using the electron beam to assess how phase segregation influences their optical behavior. Before phase segregation, monochromated low-loss EELS resolves a  $\sim 2.5$  eV plasmon at the single-particle level (Fig. 1D), consistent with ensemble UV–Vis measurements (Fig. S8). Post-segregation, in a particle with segregated Ru-rich regions at both ends (Fig. 3G), we observe the Au surface plasmon at 2.5 eV persists within the Ru-rich domains, exhibiting slight spectral broadening at the Au–Ru interface (Fig. 3H). We also observe an additional electron energy loss feature between 10–11 eV that is strongly localized to the Ru-rich regions (Fig. 3I). Electronic loss-function calculations based on bulk Ru refractive index data identify this feature as a Ru bulk plasmon (Fig. S9) (38), consistent with experimental observations (39). In a second particle with less symmetric Ru regions, spatial maps more clearly reveal an inverse relationship between the Au and Ru plasmonic responses (Fig. 3J). The Au surface plasmon is strongest in Au-rich regions, while the Ru plasmon predominantly localizes to Ru-rich domains (Fig. 3K, L). Within Ru-segregated regions, the Au plasmon is concurrently damped, yielding a clear spatial anticorrelation between Au and Ru plasmonic responses (Fig. S10). The faint edge-adjacent Ru-plasmon intensity is consistent with plasmon delocalization and edge-enhanced inelastic scattering in low-loss EELS, compounded by convolution with the SiN support. Collectively, these measurements indicate that Au–Ru phase segregation reshapes the plasmonic landscape, introducing a highly localized deep-UV Ru plasmon and attenuating the Au plasmon in Ru-rich regions, with direct implications for plasmon-mediated catalysis.

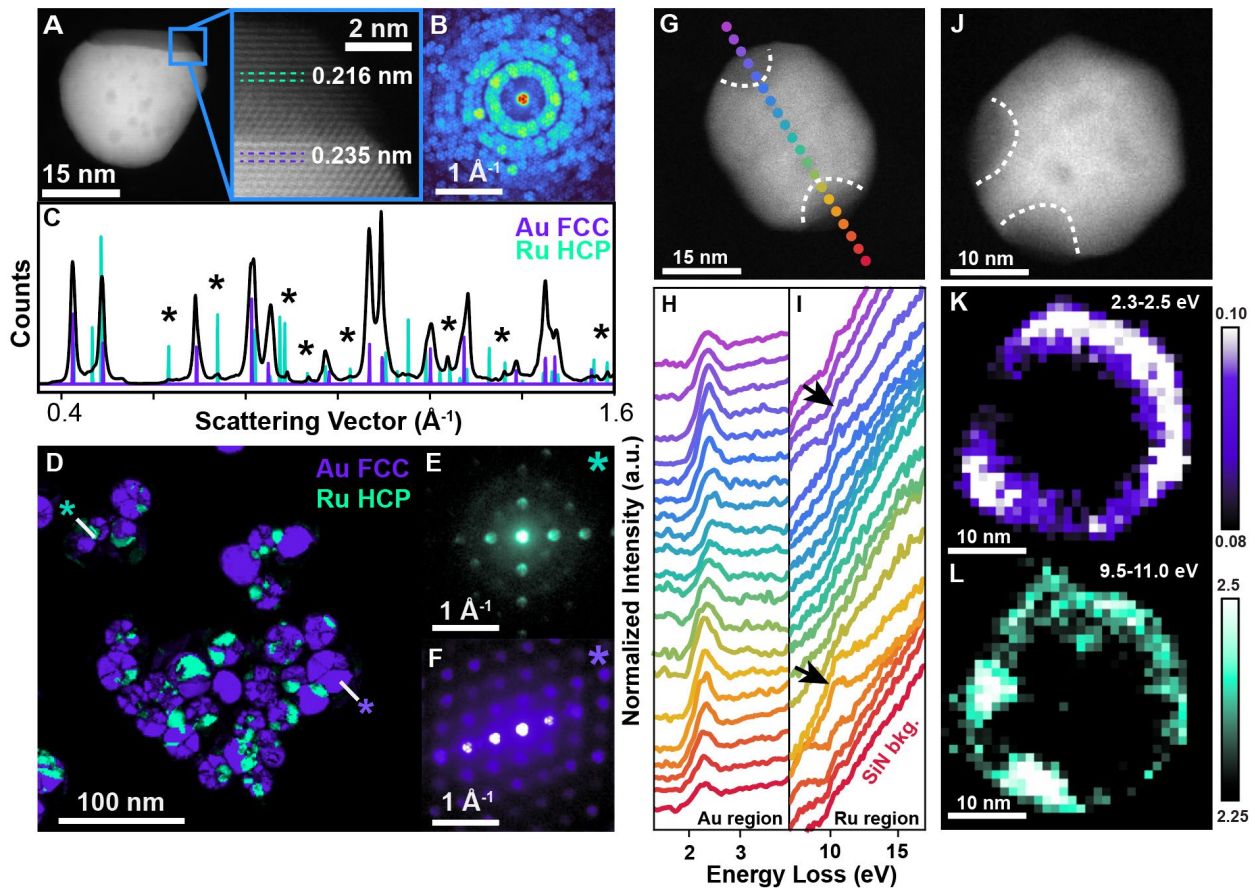


**Fig. 3. Crystallographic phase segregation and plasmonic reconfiguration in Au–Ru nanocatalysts following vacuum annealing.** (A) Atomic-resolution HAADF-STEM image of a representative phase-segregated Au–Ru nanocatalyst after vacuum annealing. Inset highlights lattice spacings corresponding to Ru HCP {0002} (0.216 nm) and Au FCC {111} (0.235 nm), consistent with intraparticle phase segregation. (B) Accumulated maximum diffraction pattern from 4D-STEM scan showing the patterned aperture and presence of mixed FCC and HCP phases. (C) Integrated powder diffraction histogram compiled from 4D-STEM data across all particles, resolving reflections from Au FCC (purple) and Ru HCP (green) phases (\* denote prominent Ru HCP peaks). (D) Phase map generated by ACOM for 20+ particles, showing spatial distribution of Ru HCP (green) and Au FCC (purple) domains. (E, F) Representative single-point diffraction patterns indexed to Ru HCP (E) and Au FCC (F) regions marked in (D); phase-matching shown in Fig. S6,7. (G) HAADF-STEM image with an overlaid monochromated EELS linescan acquired across a phase-segregated particle; dashed white outlines indicate Ru-rich regions identified by Z-contrast. (H) Corresponding low-loss EELS spectra extracted along the linescan in (G), showing the Au surface plasmon near 2.5 eV, with enhanced intensity at particle edges, which attenuates slightly in Ru regions. (I) Similarly processed EELS spectra identify a Ru plasmon near 11 eV, which lies atop the SiN background yet remains predominantly localized to Ru-rich regions at the particle edges. (J) HAADF-STEM image of a second particle containing two asymmetric Ru-rich domains (dashed outlines), used for spatial plasmon mapping. (K, L) Integrated plasmon intensity maps for two energy windows (2.3–2.5 eV for Au and 9.5–11.0 eV for Ru), revealing the spatial distribution of the Au and Ru plasmonic response.

## Atmospheric pressure unlocks a distinct restructuring regime under H<sub>2</sub>:N<sub>2</sub>

To probe how gas environments modulate catalyst evolution, we employ *in situ* gas-cell HAADF-STEM and reveal pressure-dependent restructuring pathways at atmospheric pressure of H<sub>2</sub>:N<sub>2</sub> (3:1) that are not accessible at lower pressures. As in our vacuum experiments, we heat the catalysts in gas environments at various pressures at a rate of 20 °C/min from room temperature to 150 °C, then continue in 100 °C increments with 10-min isothermal holds at each set point. We operate the gas cell under continuous flow (~0.1 sccm) to maintain a steady-state chemical environment and further mimic realistic reactor conditions. HAADF-STEM's reliance on incoherent high-angle scattering provides high-contrast imaging through the gas-cell's SiN membranes and gas environment, enabling particle visualization across pressures ranging from 50 to 782 Torr (Fig. 4A–C).

We find that low pressures (50 Torr; 0.07 atm) of H<sub>2</sub>:N<sub>2</sub> (3:1) preserve the catalyst's temperature-driven restructuring pathway observed in vacuum annealing, with rounding of the particles' facets starting at 350 °C and Au–Ru phase segregation emerging at 450 °C (Fig. 4A). Increasing the pressure to 350 Torr (0.46 atm) does not change catalyst evolution (Fig. 4B). Facet rounding and segregation proceed similarly to the low-pressure case, with only a slight increase in facet definition within Ru-segregated regions. The final catalyst morphology remains comparable to that observed after vacuum annealing. We quantify changes in catalyst size at each temperature using Otsu's thresholding to find particle area (Fig. 4D–F) (40). (See Supplementary Methods). While particle size remains constant at 50 Torr (Fig. 4D), a modest 5 ± 1% decrease is observed at 350 Torr (Fig. 4E). This change is primarily attributed to morphological evolution altering the particle's projected 2D area. However, a contribution from hydrogen-etching cannot be excluded.

In contrast to these lower pressures, the introduction of an atmospheric pressure (782 Torr /1.03 atm) H<sub>2</sub>:N<sub>2</sub> gas environment unlocks a distinct pressure-temperature regime (Fig. 4C). Qualitatively, the particle facets remain sharply defined rather than rounding with increased temperature. Quantitatively, the particle size begins to increase at 550 °C and expands by 23 ± 2% by 750 °C relative to its room-temperature size (Fig. 4C). This size increase coincides with the appearance of a central dark-contrast feature that emerges at 650 °C and continues to grow to 750 °C. Based on HAADF-STEM alone, this feature is consistent with an internal nanovoid and is confirmed by X-EDS with an absence of both Au L $\alpha$  and M $\alpha$  or Ru K $\alpha$  and L $\alpha$  x-ray lines in the center of the nanocrystal (Fig. 4G). Au–Ru phase segregation does occur as in previous particles, initiating between 350°C and 450 °C and notably preceding nanovoid nucleation. Only 1 of the 14 particles we observe *in situ* exhibits this behavior. However, post-characterization analysis indicates that roughly 5-10% of particles outside the viewing window underwent nanovoid formation (Figs. S11, S12), suggesting a pathway sensitive to particle-particle variation (e.g. size, initial composition, and grain boundaries). Additional *in situ* pressure series are shown in Fig. S13–15.

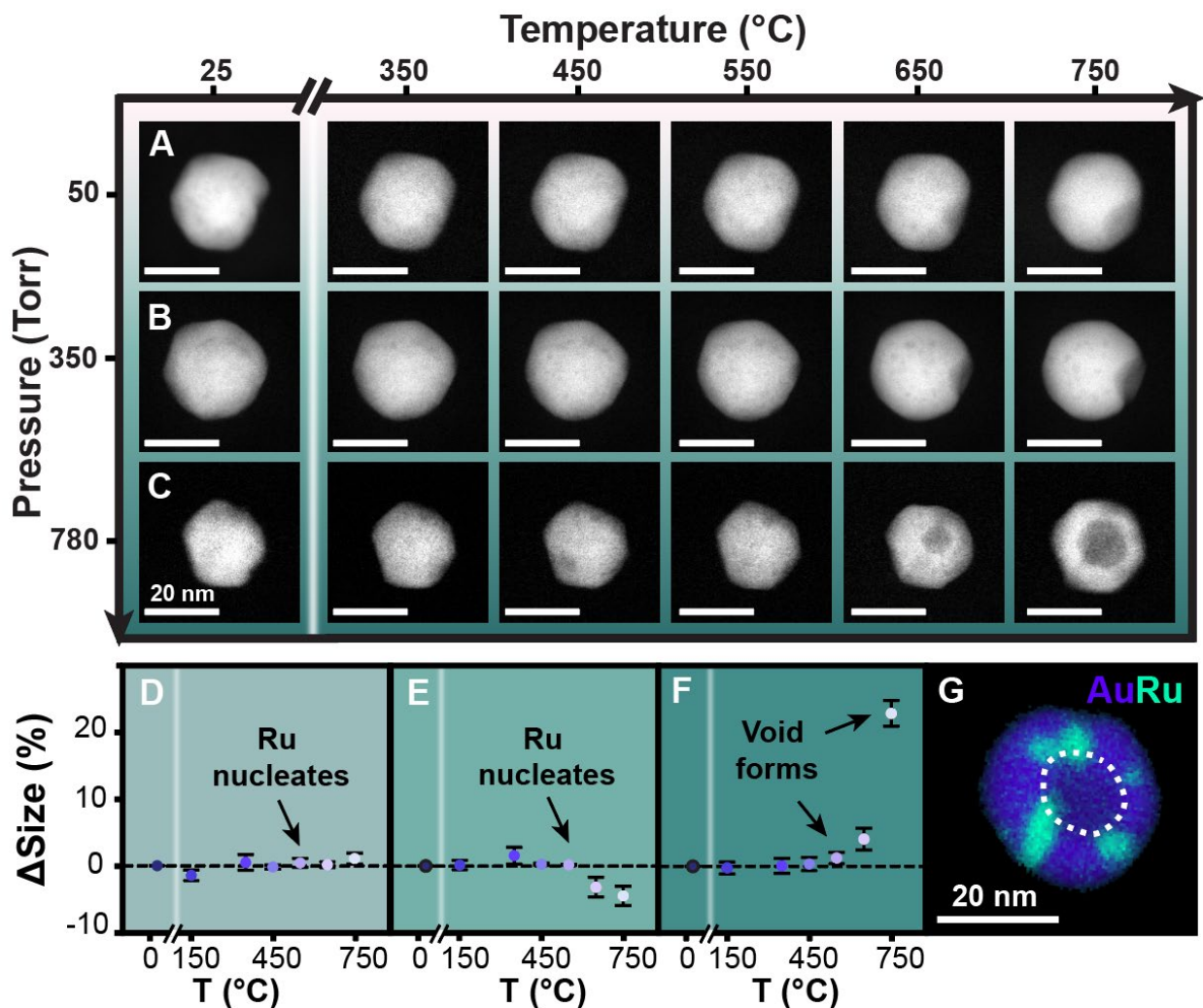


**Fig. 4. *In situ* gas-cell imaging of pressure-dependent restructuring in AuRu nanocatalysts in a H<sub>2</sub>:N<sub>2</sub> (3:1) gas environment.** (A-C) STEM-HAADF sequences of three representative Au–Ru nanocrystals acquired during stepwise heating to 750 °C in 100 °C increments in a H<sub>2</sub>:N<sub>2</sub> (3:1) gas mixture. (A) At 50 Torr (0.07 atm), Au–Ru phase segregation resembles that of vacuum annealing; see Fig. 2A. (B) At 350 Torr (0.46 atm), progressive Au–Ru phase segregation persists with slightly more pronounced faceting on the Ru-rich region. (C) At 782 Torr (~1.0 atm), a central dark-contrast feature emerges around 650 °C and continues to grow as the nanocatalyst is heated to 750 °C, accompanied by concurrent particle expansion. (D-F) Percent change in particle size as a function of temperature at 50 Torr (D), 350 Torr (E), and 782 Torr (F), relative to initial particle size. (G) X-EDS elemental map of the particle in (C) showing Au (purple) and Ru (green) phase segregation and the absence of Au La/M $\alpha$  and Ru K $\alpha$ /L $\alpha$  peaks from the dashed central region, consistent with a central nanovoid.

## Hydrogen activates nanovoid formation via a gas-mediated Kirkendall mechanism

To isolate the chemical drivers behind nanovoid formation, we first anneal AuRu nanoparticles in pure Ar at 1 atm (Fig. 5A). Under established temperature ramping, we observe restructuring pathways in Ar that match those in vacuum and low-pressure H<sub>2</sub>:N<sub>2</sub> (3:1), with Au–Ru phase segregation beginning around 450–550 °C to produce the post-heating morphology shown in Fig. 5A. These Ar gas results show that neither elevated pressure, nor beam-generated radiolytic gas species are sufficient to induce nanovoid formation (41), indicating a chemistry-specific mechanism. To identify the active species, we repeat the annealing step independently in pure N<sub>2</sub> and H<sub>2</sub> at 1 atm (Fig. 5B, C). N<sub>2</sub> annealing reveals similar segregation behavior to Ar, with no observable nanovoid formation (Fig. 5B). In stark contrast, ambient-pressure H<sub>2</sub> activates a restructuring pathway that parallels that of the high-pressure H<sub>2</sub>:N<sub>2</sub> (3:1), with many nanocrystals showing nanovoid formation (Fig. 5C). Nanovoid formation is confirmed by post-reaction X-EDS mapping of the Au (L $\alpha$ ) and Ru (K $\alpha$ ) peaks, which also highlight the proximity of Ru-rich regions with the nanovoid’s center (Fig. 5D). Across both pure H<sub>2</sub> and H<sub>2</sub>:N<sub>2</sub> (3:1) environments, nanovoids consistently adopt near-faceted geometries that exhibit a recurring intersection with Ru-rich regions (Fig. S11–12).

In order to resolve how Ru-rich regions intersect nanovoids, we apply a 2D-to-3D pipeline that feeds a HAADF-STEM tilt series of the 1 atm H<sub>2</sub>:N<sub>2</sub> annealed particle from Fig. 4C into a machine-learning (ML) accelerated tomographic reconstruction algorithm (42). The ML component compensates for the missing wedge imposed by the ±40° tilt limit of the *in situ* grid, minimizing elongation artifacts in the reconstructed particle (Fig. 5E, F, and Fig. S17). Three-dimensional isosurface rendering of this machine-learning-assisted tomographic reconstruction shows the particle exterior (blue) and internal low-density features (red) (Fig. 5F). The reconstruction reveals a through-thickness nanovoid intersecting two free surfaces (axial view), together with a branched internal channel extending along the y-axis (side view). As vacuum and Ru-rich regions both exhibit reduced contrast, this channel is assigned via co-registration with the HAADF-STEM tilt series and X-EDS map (Fig. 4G), confirming its Ru-rich nature (Fig. S18). Orthogonal slices along the nanovoid axis of the reconstruction further resolve the direct intersection between this low-contrast Ru-rich channel and dark-contrast nanovoid (Fig. 5G).

Although the reconstructed nanovoid in Fig. 5F is through-thickness, this geometry is not universal. Applying the same tomographic workflow to a second void-containing particle reveals an entirely internal, off-center cavity (Fig. S19, S20). Across all voided particles, tomography, HAADF-STEM, and X-EDS analyses indicate the presence of both smaller, fully internal nanovoids and nanovoids that extend to free surfaces.

Our combined gas-specific annealing experiments and 3D reconstructions establish two key constraints for any mechanism of nanovoid formation. First, nanovoid formation is strictly hydrogen-dependent. Under standard preparation conditions, nanovoids form only in H<sub>2</sub>-

containing environments at partial pressures  $\geq 0.75$  atm. They are not observed under vacuum or inert gases, despite comparable Au–Ru phase segregation across all conditions. Second, nanovoids consistently nucleate within the particle and intersect Ru-rich domains, indicating an internal origin at the Au/Ru interface rather than surface etching or volatilization. Notably, prior *in situ* studies report no nanovoid formation in pure Au nanocrystals under 1 atm H<sub>2</sub> at elevated temperatures, underscoring the necessity of Au–Ru interfaces for nanovoid nucleation (43).

These features differ from the classical nanoscale Kirkendall effect, where oxidation in metallic systems or galvanic replacement produces hollow particles (44–46). Oxidation and loss of Ru via volatile RuO<sub>x</sub> can be excluded, as RuO<sub>x</sub> reduces to metallic Ru at H<sub>2</sub> pressures as low as 4.5 Torr at 250 °C, well below the conditions of our 50 Torr experiment, where nanovoids are not observed (47, 48). They also differ from some bimetallic cases in which pure annealing drives interface-trapped nanovoids through asymmetric vacancy formation energies (49–51). Here, identical thermal conditions are insufficient. Nanovoids are observed to emerge *only* under high-pressure H<sub>2</sub>.

One possible explanation is that initial Au–Ru phase nucleation establishes internal metal/metal interfaces that enable asymmetric interdiffusion, with continued Au/Ru interdiffusion driving vacancy accumulation. Transition state calculations on a large-scale Au/Ru interface model using a DFT-trained machine-learning interatomic potential (MLIP) quantify this asymmetry, yielding diffusion energy barriers of 0.41 eV for Au in Ru and 0.23 eV for Ru in Au. Under inert or vacuum conditions, we propose that this weaker asymmetry maintains vacancies at low equilibrium concentrations, where they are efficiently annihilated at free surfaces, suppressing nanovoid nucleation. In the presence of adsorbed hydrogen, the diffusion barriers change to 0.87 eV and 0.18 eV, respectively. Thus, hydrogen amplifies Au–Ru diffusion asymmetry, a hallmark of bimetallic Kirkendall processes (44, 49, 52, 53), promoting vacancy clustering and nanovoid nucleation at internal interfaces. Atomic hydrogen is also expected to stabilize vacancies and increase their mobility, particularly in Ru-rich regions where hydrogen solubility is higher (54, 55). The consistent void–Ru co-localization supports such an interface-mediated mechanism.

To further elucidate the impact of H on the structural evolution, we perform grand canonical Monte Carlo (GCMC) simulations on a large-scale slab model of the FCC AuRu alloy (1:0.2), allowing for both metal rearrangement and H exchange with a reservoir at fixed chemical potential. Under H<sub>2</sub>-free conditions, GCMC-simulated H-coverage quickly converges to zero on both the surface and sub-surface (Fig. S23). Under 1 atm H<sub>2</sub> conditions, Ru aggregates at the surface are stabilized by high local H coverage, with some H permeating the Ru region’s sub-surface (Fig. S23). Notably, bulk Ru hydrides do not form under these pressures (56), indicating local hydrogen stabilization rather than hydride-phase formation.

Given that volatile Ru oxides are not stable under the reducing conditions used here (48), and that nanovoids are observed only in the presence of hydrogen, our results reveal a distinct

variant of the Kirkendall effect in which gas-phase hydrogen controls vacancy accumulation and nanovoid nucleation. To our knowledge, this represents the first *in situ* demonstration that hydrogen pressure can regulate vacancy-mediated nanovoid formation in multimetallic nanoparticles. These findings extend the Kirkendall framework to regimes in which reactive gases influence vacancy kinetics rather than chemical conversion and highlight a new pathway for nanovoid generation in alloy nanoparticles under catalytic conditions.

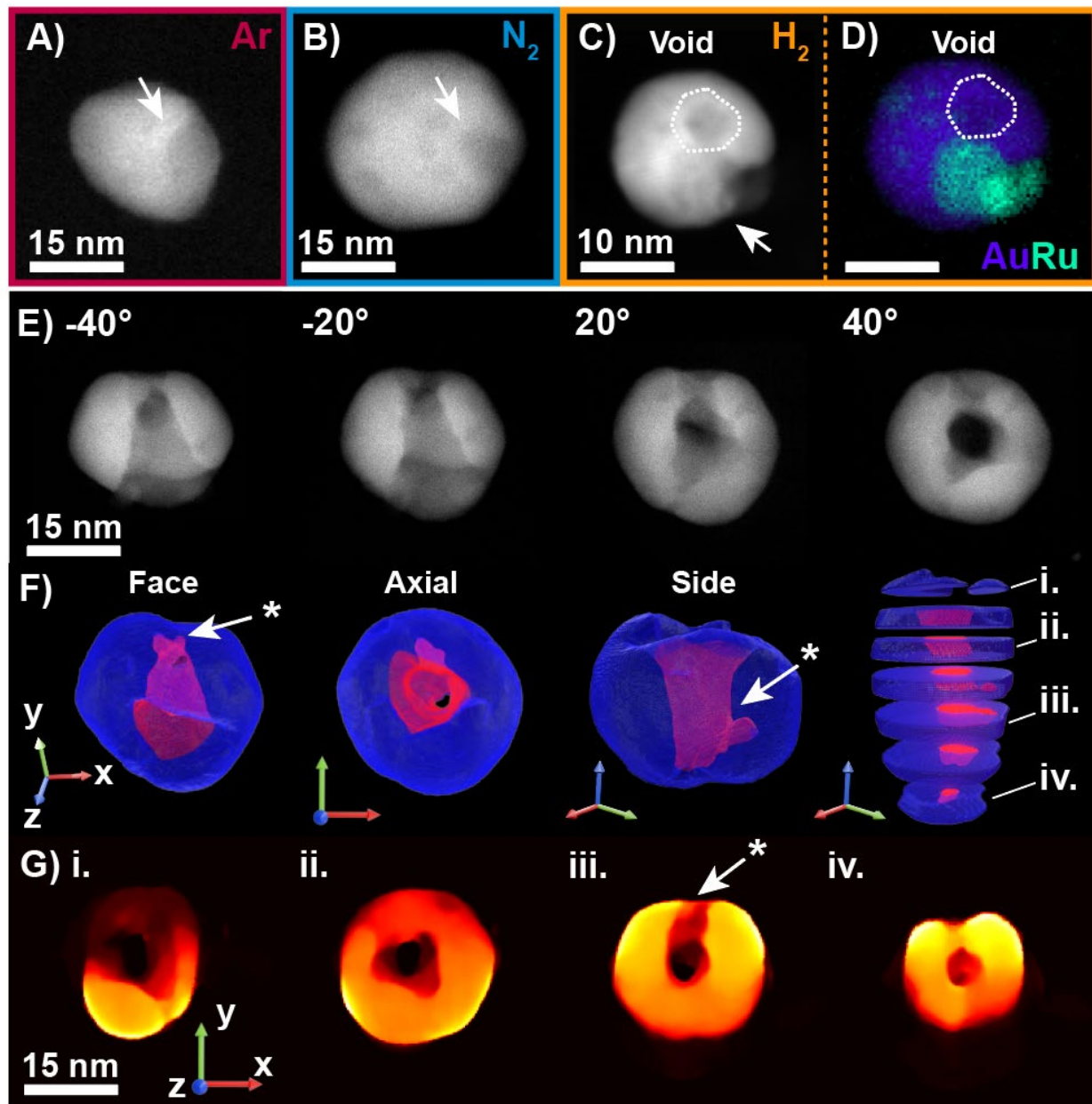


**Fig. 5. Hydrogen drives nanovoid nucleation in Au–Ru nanoparticles.** (A–C) HAADF-STEM images of representative Au–Ru nanoparticles heated to 750 °C in Ar (A), N<sub>2</sub> (B), and H<sub>2</sub> (C) at 1 atm, and dashed outlines mark Ru-rich domains. Pronounced nanovoid formation emerges only under H<sub>2</sub>. (D) X-EDS maps

of the particle in (C) show Au–Ru segregation and a complete absence of Au (L $\alpha$ ) and Ru (K $\alpha$ ) counts in the dashed central region, consistent with an internal nanovoid. (E) HAADF-STEM tilt series of the particle from Fig. 4C after reaction, showing that the void extends through the whole particle. (F) Machine-learning-assisted tomographic reconstruction from multiple viewing directions reveals the catalyst's internal cavity (red) and exterior (blue) 3D geometry. (G) Orthogonal tomographic slices reveal that the cavity tapers asymmetrically along the length of the particle. Intensity reflects reconstructed voxel values. (F–G) White arrows indicate a low-contrast side channel, attributed to Ru.

In summary, we performed correlated *in situ* and multimodal measurements to reveal temperature, pressure, and chemical stimuli that govern AuRu nanocatalyst stability and restructuring under realistic conditions. Polycrystalline AuRu nanocatalysts with Au/Ru intermixing exhibit an FCC structure. At elevated temperatures, the nanocatalysts phase-segregate into distinct Au (FCC) and Ru (HCP) regions through a thermally driven pathway. When a H<sub>2</sub>:N<sub>2</sub> (3:1) gas environment is introduced, and the pressure is increased to 1 atm, a previously inaccessible restructuring regime emerges, characterized by sharp faceting and selective nanovoid formation. By systematically varying the chemical environment from inert Ar/N<sub>2</sub> to H<sub>2</sub>, we identify H<sub>2</sub> as the dominant chemical driver of this restructuring. Mechanistically, diffusion barriers calculated using DFT-trained machine-learning potentials suggest that H<sub>2</sub> enhances asymmetric Au/Ru diffusion at the Au–Ru interface post-phase segregation. This gas-modulated diffusion asymmetry promotes vacancy accumulation, revealing a hydrogen-activated variant of the nanoscale Kirkendall effect that governs nanovoid formation.

Our results demonstrate that closing the pressure gap between real-world conditions and *in situ* ammonia studies is essential for revealing dynamic behavior that arises only under near-native environments. We show that gas-mediated modulation of Au/Ru diffusion asymmetry provides a chemically addressable pathway to access nanoscale Kirkendall-type restructuring, offering a new lever for nanomaterial design. Integrating additional external stimuli, such as optical excitation, may further expand this design space, uncovering regenerative or self-stabilizing behaviors (57). More broadly, the multimodal and multidimensional electron microscopy framework applied here provides a systematic strategy for disentangling coupled thermal, pressure, and chemical driving forces in complex materials. This approach is extensible beyond catalysis to other energy-relevant systems, including battery electrodes, hydrogen-storage media, and carbon-capture materials, where performance and lifetime are governed by dynamic evolution under reactive environments.

## Acknowledgements

The authors acknowledge Pinaki Mukherjee for TEM assistance and all members of the Dionne group for their scientific feedback and support. **Funding:** J.A.D., A.S.M.-G., and P.M. acknowledge salary support from the Office of Basic Energy Sciences, US Department of Energy, Division of Materials Science and Engineering, DE-AC02-76SF00515. We also acknowledge the financial support from the U.S. Department of Energy Office of Science National Quantum

Information Science Research Centers as part of the Q-NEXT center, which provided support for the multimodal TEM instrumentation. A.S.M.-G. acknowledges the support of the National Science Foundation Graduate Research fellowship (NSF-GRFP) under grant no. DGE-2146755 and the John Stauffer Graduate Fellowship. This research used resources of the National Energy Research Scientific Computing Center, a DOE Office of Science User Facility supported by the Office of Science of the U.S. Department of Energy under Contract No.361 DE-AC02-05CH11231 using AI4Sci@NERSC NERSC award NERSC DDR-ERCAP0038157 and BES-ERCAP0024127. Z.Z. is supported by the Stanford Energy Fellowship from the Precourt Institute for Energy, Doerr School of Sustainability. F.A-P. acknowledges support from the U.S. Department of Energy, Office of Science, Office of Basic Energy Sciences, Chemical Sciences, Geosciences, and Biosciences Division, Catalysis Science Program to the SUNCAT Center for Interface Science and Catalysis. Part of this work was performed at nano@stanford RRID:SCR\_026695. **AI declaration:** This paper has been proofread by a language model (ChatGPT, OpenAI), and the authors have consulted the output and edited the paper wherever deemed appropriate. All scientific content, interpretations, and conclusions are the authors' own.

## References

1. J. W. Erisman, M. A. Sutton, J. Galloway, Z. Klimont, W. Winiwarter, How a century of ammonia synthesis changed the world. *Nat. Geosci.* **1**, 636–639 (2008).
2. A. Vojvodic, A. J. Medford, F. Studt, F. Abild-Pedersen, T. S. Khan, T. Bligaard, J. K. Nørskov, Exploring the limits: A low-pressure, low-temperature Haber–Bosch process. *Chem. Phys. Lett.* **598**, 108–112 (2014).
3. Y. Gao, A. Cabrera Serrenho, Greenhouse gas emissions from nitrogen fertilizers could be reduced by up to one-fifth of current levels by 2050 with combined interventions. *Nat. Food* **4**, 170–178 (2023).
4. Z.-H. Xue, S.-N. Zhang, Y.-X. Lin, H. Su, G.-Y. Zhai, J.-T. Han, Q.-Y. Yu, X.-H. Li, M. Antonietti, J.-S. Chen, Electrochemical reduction of N<sub>2</sub> into NH<sub>3</sub> by donor-acceptor couples of Ni and Au nanoparticles with a 67.8% Faradaic efficiency. *J. Am. Chem. Soc.* **141**, 14976–14980 (2019).
5. M. Sun, C. Ma, M. Ma, Y. Wei, S. Dong, X. Zhang, J. Tian, M. Shao, Electrochemical ammonia synthesis via nitrogen reduction reaction on 1T/2H mixed-phase MoSSe catalyst: Theoretical and experimental studies. *Mater. Today Phys.* **30**, 100945 (2023).
6. J. Mu, X.-W. Gao, T. Yu, L.-K. Zhao, W.-B. Luo, H. Yang, Z.-M. Liu, Z. Sun, Q.-F. Gu, F. Li, Ambient electrochemical ammonia synthesis: From theoretical guidance to catalyst design. *Adv. Sci. (Weinh.)* **11**, e2308979 (2024).
7. M. Hattori, N. Okuyama, H. Kurosawa, M. Hara, Low-temperature ammonia synthesis on iron catalyst with an electron donor. *J. Am. Chem. Soc.* **145**, 7888–7897 (2023).

8. J. Wang, L. Liu, R. Li, S. Wang, X. Ju, T. He, J. Guo, P. Chen, Highly active manganese nitride-europium nitride catalyst for ammonia synthesis. *iScience* **27**, 110858 (2024).
9. F. Tian, J. Li, W. Chen, L. Tang, M. Wu, Innovative progress of thermal ammonia synthesis under mild conditions. *Int. J. Hydrogen Energy* **78**, 92–122 (2024).
10. B. Arjones-Fernández, A. Malik, L. Guillade, R. Khatua, L. V. Besteiro, A. Sousa-Castillo, M. Vázquez-González, R. A. Álvarez-Puebla, M. A. Correa-Duarte, Solar-driven Photocatalytic N<sub>2</sub> reduction to ammonia using plasmonic Au@NiZIF-8 MOF hybrids. *Adv. Opt. Mater.*, doi: 10.1002/adom.202502759 (2025).
11. I. Moriya, Converting N<sub>2</sub> molecules into NH<sub>3</sub> with TiO<sub>2</sub>/Fe<sub>3</sub>O<sub>4</sub> composite covered with a thin water layer under ambient condition. *Sci. Rep.* **13**, 7746 (2023).
12. Y. Shi, Z. Zhao, D. Yang, J. Tan, X. Xin, Y. Liu, Z. Jiang, Engineering photocatalytic ammonia synthesis. *Chem. Soc. Rev.* **52**, 6938–6956 (2023).
13. L. Liu, A. Corma, Bimetallic sites for catalysis: From binuclear metal sites to bimetallic nanoclusters and nanoparticles. *Chem. Rev.* **123**, 4855–4933 (2023).
14. S. S. S. Ganti, P. K. Roy, N. Wagh, K. N. S. Siva Sai, S. Kumar, Strategically designed catalysts for ammonia synthesis under mild conditions: recent advances and challenges. *J. Mater. Chem. A Mater. Energy Sustain.* **13**, 15361–15426 (2025).
15. T. Hou, L. Chen, Y. Xin, W. Zhu, C. Zhang, W. Zhang, S. Liang, L. Wang, Porous CuFe for plasmon-assisted N<sub>2</sub> photofixation. *ACS Energy Lett.* **5**, 2444–2451 (2020).
16. B.-H. Wang, B. Hu, G.-H. Chen, X. Wang, S. Tian, Y. Li, X.-S. Hu, H. Wang, C.-T. Au, L.-L. Jiang, L. Chen, S.-F. Yin, Plasmon-induced photocatalytic nitrogen fixation on medium-spin Au<sub>3</sub>Fe<sub>1</sub>/Mo single-atom alloy antenna reactor. *Chem Catal.* **4**, 101083 (2024).
17. L. Yuan, B. B. Bourgeois, E. Begin, Y. Zhang, A. X. Dai, Z. Cheng, A. S. McKeown-Green, Z. Xue, Y. Cui, K. Xu, Y. Wang, M. R. Jones, Y. Cui, A. Majumdar, J. L. Bao, J. A. Dionne, Atmospheric-pressure ammonia synthesis on AuRu catalysts enabled by plasmon-controlled hydrogenation and nitrogen-species desorption. *Nat. Energy*, 1–11 (2025).
18. F. Tao, M. Salmeron, Surface restructuring and predictive design of heterogeneous catalysts. *Science* **386** (2024).
19. K. D. Gilroy, A. Ruditskiy, H.-C. Peng, D. Qin, Y. Xia, Bimetallic nanocrystals: Syntheses, properties, and applications. *Chem. Rev.* **116**, 10414–10472 (2016).
20. K. Sytwu, M. Vadai, F. Hayee, D. K. Angell, A. Dai, J. Dixon, J. A. Dionne, Driving energetically unfavorable dehydrogenation dynamics with plasmonics. *Science* **371**, 280–283 (2021).
21. J. L. Vincent, P. A. Crozier, Atomic level fluxional behavior and activity of CeO<sub>2</sub>-supported Pt catalysts for CO oxidation. *Nat. Commun.* **12**, 5789 (2021).

22. K. Koo, P. J. M. Smeets, X. Hu, V. P. Dravid, Analytical in situ gas transmission electron microscopy enabled with ultrathin silicon nitride membranes. *Microsc. Microanal.* **29**, 1597–1598 (2023).

23. S. B. Simonsen, S. Dahl, E. Johnson, S. Helveg, Ceria-catalyzed soot oxidation studied by environmental transmission electron microscopy. *J. Catal.* **255**, 1–5 (2008).

24. S. Lee, K. Gadelrab, L. Cheng, J. P. Braaten, H. Wu, F. M. Ross, Simultaneous 2D projection and 3D topographic imaging of gas-dependent dynamics of catalytic nanoparticles. *ACS Nano* **18**, 21258–21267 (2024).

25. S. Janbroers, P. A. Crozier, H. W. Zandbergen, P. J. Kooyman, A model study on the carburization process of iron-based Fischer–Tropsch catalysts using in situ TEM–EELS. *Appl. Catal. B* **102**, 521–527 (2011).

26. S. B. Vendelbo, C. F. Elkjær, H. Falsig, I. Puspitasari, P. Dona, L. Mele, B. Morana, B. J. Nelissen, R. van Rijn, J. F. Creemer, P. J. Kooyman, S. Helveg, Visualization of oscillatory behaviour of Pt nanoparticles catalysing CO oxidation. *Nat. Mater.* **13**, 884–890 (2014).

27. J. Ding, L. Wang, P. Wu, A. Li, W. Li, C. Stampfl, X. Liao, B. S. Haynes, X. Han, J. Huang, Confined Ru nanocatalysts on surface to enhance ammonia synthesis: An in situ ETEM study. *ChemCatChem* **13**, 534–538 (2021).

28. M. R. Ward, R. W. Mitchell, E. D. Boyes, P. L. Gai, Visualization of atomic scale reaction dynamics of supported nanocatalysts during oxidation and ammonia synthesis using in-situ environmental (scanning) transmission electron microscopy. *J. Energy Chem.* **57**, 281–290 (2021).

29. L. Österlund, Pressure Gaps in Heterogeneous Catalysis. Wiley [Preprint] (2021). <https://doi.org/10.1002/9783527813599.ch13>.

30. H. Okamoto, T. B. Massalski, The Au-Ru (gold-ruthenium) system. *Bull. Alloy Phase Diagrams* **5**, 388–390 (1984).

31. Q. Zhang, K. Kusada, D. Wu, T. Yamamoto, T. Toriyama, S. Matsumura, S. Kawaguchi, Y. Kubota, H. Kitagawa, Selective control of fcc and hcp crystal structures in Au-Ru solid-solution alloy nanoparticles. *Nat. Commun.* **9**, 510 (2018).

32. T. Chookajorn, H. A. Murdoch, C. A. Schuh, Design of stable nanocrystalline alloys. *Science* **337**, 951–954 (2012).

33. mp-33: Ru (Hexagonal, P6\_3/mmc, 194), *Materials Project*. <https://next-gen.materialsproject.org/materials/mp-33>.

34. mp-81: Au (cubic, Fm-3m, 225). <https://legacy.materialsproject.org/materials/mp-81/>.

35. Y. Jiang, Z. M. Wong, H. Yan, T. L. Tan, U. Mirsaidov, Revealing multistep phase separation in metal alloy nanoparticles with in situ transmission electron microscopy. *ACS*

*Nano* **19**, 3886–3894 (2025).

36. S. E. Zeltmann, A. Müller, K. C. Bustillo, B. Savitzky, L. Hughes, A. M. Minor, C. Ophus, Patterned probes for high precision 4D-STEM bragg measurements. *Ultramicroscopy* **209**, 112890 (2020).
37. C. Ophus, S. E. Zeltmann, A. Bruefach, A. Rakowski, B. H. Savitzky, A. M. Minor, M. C. Scott, Automated crystal orientation mapping in py4DSTEM using sparse correlation matching. *Microsc. Microanal.* **28**, 1–14 (2022).
38. J. T. Cox, G. Hass, J. B. Ramsey, W. R. Hunter, Reflectance and optical constants of evaporated ruthenium in the vacuum ultraviolet from 300 to 2000 Å. *J. Opt. Soc. Am.* **64**, 423 (1974).
39. C. Hébert, W.-D. Schöne, D. S. Su, Experimental and theoretical determination of low electron energy loss spectra of Ag and Ru. *Ultramicroscopy* **106**, 1115–1119 (2006).
40. N. Otsu, A threshold selection method from gray-level histograms. *IEEE Trans. Syst. Man Cybern.* **9**, 62–66 (1979).
41. K. Koo, N. S. Chellam, S. Shim, C. A. Mirkin, G. C. Schatz, X. Hu, V. P. Dravid, Electron-induced radiation chemistry in environmental transmission electron microscopy, *arXiv [cond-mat.mtrl-sci]* (2024). <http://arxiv.org/abs/2402.17928>.
42. C. Lim, C. Casert, A. R. C. McCray, S. Lee, A. Barnum, J. Dionne, C. Ophus, Missing wedge inpainting and joint alignment in electron tomography through implicit neural representations, *arXiv [eess.IV]* (2025). <https://doi.org/10.48550/arXiv.2512.08113>.
43. A. Chmielewski, J. Meng, B. Zhu, Y. Gao, H. Guesmi, H. Prunier, D. Alloyeau, G. Wang, C. Louis, L. Delannoy, P. Afanasiev, C. Ricolleau, J. Nelayah, Reshaping dynamics of gold nanoparticles under H<sub>2</sub> and O<sub>2</sub> at atmospheric pressure. *ACS Nano* **13**, 2024–2033 (2019).
44. Y. Yin, R. M. Rioux, C. K. Erdonmez, S. Hughes, G. A. Somorjai, A. P. Alivisatos, Formation of hollow nanocrystals through the nanoscale Kirkendall effect. *Science* **304**, 711–714 (2004).
45. Z. Yang, N. Yang, M.-P. Pilani, Nano Kirkendall effect related to nanocrystallinity of metal nanocrystals: Influence of the outward and inward atomic diffusion on the final nanoparticle structure. *J. Phys. Chem. C Nanomater. Interfaces* **119**, 22249–22260 (2015).
46. S. W. Chee, S. F. Tan, Z. Baraissov, M. Bosman, U. Mirsaidov, Direct observation of the nanoscale Kirkendall effect during galvanic replacement reactions. *Nat. Commun.* **8** (2017).
47. S. Carenco, C. Sasso, M. Faustini, P. Eloy, D. P. Debecker, H. Bluhm, M. Salmeron, The active state of supported ruthenium oxide nanoparticles during carbon dioxide methanation. *J. Phys. Chem. C Nanomater. Interfaces* **120**, 15354–15361 (2016).
48. G. Fraga, M. Konarova, L. Massin, A. D. K. Deshan, D. Rackemann, B. Laycock, S. Pratt,

N. Batalha, Reduction of RuO<sub>2</sub> nanoparticles supported on silica by organic molecules: a strategy for nanoparticle redispersion. *J. Mater. Chem. A Mater. Energy Sustain.* **13**, 7445–7460 (2025).

- 49. S. W. Chee, Z. M. Wong, Z. Baraissov, S. F. Tan, T. L. Tan, U. Mirsaidov, Interface-mediated Kirkendall effect and nanoscale void migration in bimetallic nanoparticles during interdiffusion. *Nat. Commun.* **10**, 2831 (2019).
- 50. G. Glodán, C. Cserháti, I. Beszeda, D. L. Beke, Production of hollow hemisphere shells by pure Kirkendall porosity formation in Au/Ag system. *Appl. Phys. Lett.* **97**, 113109 (2010).
- 51. G. Glodán, C. Cserháti, D. L. Beke, Temperature-dependent formation and shrinkage of hollow shells in hemispherical Ag/Pd nanoparticles. *Philos. Mag. (Abingdon)* **92**, 3806–3812 (2012).
- 52. A.-A. El Mel, R. Nakamura, C. Bittencourt, The Kirkendall effect and nanoscience: hollow nanospheres and nanotubes. *Beilstein J. Nanotechnol.* **6**, 1348–1361 (2015).
- 53. B. D. Anderson, J. B. Tracy, Nanoparticle conversion chemistry: Kirkendall effect, galvanic exchange, and anion exchange. *Nanoscale* **6**, 12195–12216 (2014).
- 54. R. B. McLellan, Solid solutions of hydrogen in gold, silver and copper. *J. Phys. Chem. Solids* **34**, 1137–1141 (1973).
- 55. R. B. McLellan, W. A. Oates, The solubility of hydrogen in rhodium, ruthenium, iridium and nickel. *Acta Metall.* **21**, 181–185 (1973).
- 56. M. A. Kuzovnikov, M. Tkacz, Synthesis of ruthenium hydride. *Phys. Rev. B.* **93** (2016).
- 57. Y. Yuan, J. Zhou, A. Bayles, H. Robatjazi, P. Nordlander, N. J. Halas, Steam methane reforming using a regenerable antenna–reactor plasmonic photocatalyst. *Nat. Catal.* **7**, 1339–1349 (2024).

## Materials and Methods

### Nanocrystals Synthesis and Sample Preparation

Bimetallic AuRu alloy nanocrystals were synthesized using a polyol reduction method with native polyvinylpyrrolidone (PVP) ligands, as described by Yuan et al. (1). The average particle size was found to be  $25 \pm 6$  nm.

S/TEM samples were prepared by drop-casting 5  $\mu\text{L}$  of a dilute AuRu aqueous solution onto a TEM grid and air-drying for  $\geq 12$  hrs. On-chip ligand removal was performed by dipping the particle-coated grids in an aqueous 20 mM sodium borohydride (NaBH<sub>4</sub>, Fisher) solution (10

s for carbon-coated grids, 30 s for SiN grids), cold water (10 s), and IPA (10 s). This method significantly reduced observed carbon contamination by removing the nanocrystals' native PVP ligands.

## **Electron Microscopy**

STEM characterization was performed using a probe-corrected Thermo Fisher Spectra 300 operating at 300 kV. TEM imaging was conducted on an aberration-corrected Thermo Fisher Titan environmental transmission electron microscope, also operating at 300 kV.

### ***In situ* Imaging**

#### *STEM*

Probe-corrected STEM images were acquired using a spot size of 9, probe semi-angle of 30 mrad, and an incident beam current of 100 pA. A high-angle annular dark field (HAADF) detector with detection half-angles spanning from 63 to 200 mrad was employed.

#### *HRTEM*

Aberration-corrected high-resolution transmission electron microscopy (HRTEM) imaging was performed with a maximum electron dose rate of  $800 \text{ e- } \text{\AA}^{-2} \text{ s}^{-1}$  using a Gatan OneView SI CMOS camera. Live drift correction was employed to enable lattice resolution at elevated temperatures.

## ***In situ* Experiments**

### *Chip preparation*

*In situ* chips were subjected to 3 min of O<sub>2</sub> plasma cleaning prior to dropcasting and ligand removal with NaBH<sub>4</sub>. In the case of the top and bottom chips for the gas cell, the top chip was plasma cleaned for 60 s post-NaBH<sub>4</sub> ligand removal.

### *Vacuum Annealing*

S/TEM annealing experiments were carried out using a Protobricks Aduro 500 Heating Holder with MEMS-based, carbon-coated grids. For the STEM annealing data in Figure 2a, the samples were annealed from 150 °C to 650 °C in 50 °C increments at a ramp rate of 20 °C/min. At each Δ50 °C temperature point, the sample was allowed to equilibrate for 5 minutes and then imaged for an additional ~5 min. The sample was then rapidly cooled back to room temperature. A similar procedure was followed for TEM vacuum annealing, with a ramp rate of 15 °C/min and a maximum temperature of 750 °C.

MEMS-based silicon nitride (SiN) grids were used for monochromated STEM-EELS to allow observation of the gold (Au) plasmon. To further remove volatile surface contaminants, samples first underwent 1 hr of beam showering (5.6 nA screen current,  $\sim 50 \mu\text{m} \times 50 \mu\text{m}$  illuminated area). Annealing was performed from 350 °C to 750 °C in 100 °C increments using a 20 °C/min ramp rate. Following each 100 °C step, the sample was allowed to equilibrate for  $\geq 10$  min before being ramped to the next temperature. Low-loss STEM-EELS spectra were collected after rapid cooling of the sample to room temperature to improve stability.

### *Gas-phase reaction*

Gas-phase experiments were conducted using a Protochips Atmosphere holder with a 3:1 H<sub>2</sub> (6.0 purity, Praxair) to N<sub>2</sub> (5.0 purity, Linde) gas mixture at pressures ranging from 50 to 782 Torr. The gas cell consisted of two 50 nm-thick SiN MEMS chips (top and bottom) separated by a 5  $\mu\text{m}$  spacer. The sample was drop-cast onto the top chip, ligand stripped using the NaBH<sub>4</sub> procedure, and O<sub>2</sub> plasma cleaned for 60 s. After gas cell assembly and holder insertion into the microscope, the sample underwent 10 pump/purge cycles with inert argon gas, achieving a maximum pump pressure of 760 Torr and minimum purge pressure of 1 Torr. This process serves to remove volatile organic and oxidative species from the gas cell.

*In-situ* annealing was performed at each gas pressure using a 20 °C/min temperature ramp rate. The sample was allowed to equilibrate for 5 min before being imaged at 150, 350, 450, 550, 650, and 750 °C. Post-annealing, the sample was rapidly cooled to room temperature in the same 3:1 H<sub>2</sub>:N<sub>2</sub> environment for further characterization.

## **Post-reaction characterization**

### *Atomic STEM Imaging*

Probe-corrected STEM images were acquired using a spot size of 9, probe semi-angle of 24 mrad, and an incident beam current of 50 pA. A high-angle annular dark field (HAADF) detector with detection half-angles spanning from 63 to 200 mrad was employed to collect 4096 x 4096 pixel images, with dwell times ranging from 100 to 500 ns.

### *X-EDS Spectral Image Acquisition*

X-ray energy dispersive spectroscopy (X-EDS) data sets were collected before and after reaction using the Protochips inspection holder, which accommodates MEMS chips from both heating and gas experiments. X-EDS maps were acquired using a spot size of 6, a probe semi-angle of 30 mrad, and an incident beam current of 130-150 pA. A SuperX energy dispersive spectroscopy detector with a 0.7 sr X-EDS solid angle was employed with a dwell time of 50  $\mu\text{s}$ . Chemical distributions were obtained using both the HyperSpy and eXSpy open-source Python packages.

## 4D STEM Nanobeam Electron Diffraction

Four-dimensional scanning transmission electron microscopy (4D STEM) was performed on the AuRu nanocrystals before and after gas reaction using a DECTRIS ARINA (Si) direct-electron detector. For the pre-reaction characterization, a 20  $\mu\text{m}$  aperture was used to obtain a nominal convergence semi-angle of 2.5 mrad and an incident beam current of 70 pA on the sample. A 256 x 256 image was acquired with a per-pixel dwell time of 500  $\mu\text{s}$ . The camera length was set to 73 mm, giving a calibrated k-space pixel size of 0.0384  $\text{\AA}^{-1}$ .

For post-reaction AuRu characterization, we employed a 10  $\mu\text{m}$  patterned bullseye aperture in order to obtain a nominal convergence semi-angle of 1.25 mrad and an incident beam current of 50 pA (2). The camera length was increased to 185 mm to allow for full resolution of the bullseye pattern, yielding a calibrated k-space pixel size of 0.0151  $\text{\AA}^{-1}$ . The fully resolved patterned aperture allows for the more precise measurement of lattice constants, which is required to distinguish Au (FCC) and Ru (HCP) phases.

## Monochromated STEM EELS Spectra and Map Acquisition

Electron energy loss spectroscopy (EELS) was performed using a monochromated EELS system equipped with a dual EELS Gatan Imaging Filter (GIF) Continuum spectrometer. The microscope was operated at 300 kV, with an incident beam current of 130-135 pA on the sample, and a probe convergence semi-angle of  $\alpha = 21.4$  mrad. All spectra were acquired with an energy dispersion of 10 meV per channel, an EELS entrance aperture of 1 mm, and a collection semi-angle of 28.0 mrad. For spectral mapping, acquisition times were set to 2.0 ms for the zero-loss peak (ZLP) and 0.8 s for the low-loss region. Linescan spectra were taken using ZLP and low-loss acquisition times of 2.0 ms and 0.5 s, respectively.

## Tomography

To perform a tomographic tilt series of the AuRu nanocrystals post-gas-phase reaction, we first beam-showered the sample in TEM mode (30 min, 5.56 nA screen current,  $\sim 50 \mu\text{m} \times 50 \mu\text{m}$  illuminated area). The microscope was operated in STEM mode with a probe convergence semi-angle of  $\alpha = 30.0$  mrad, an incident beam current of 50 pA, and detection half-angles of 63 to 200 mrad. The tilt series was conducted on *in situ* gas chips mounted in the Protochips inspection holder, which constrained the tilt range to  $\pm 40^\circ$ . Images at both  $0^\circ$  and  $90^\circ$  scan rotations were taken at  $2^\circ$  intervals to minimize the presence of scan defects upon reconstruction.

## Computational details

The dataset for training the machine learning interatomic potential (MLIP) is generated using the GOCIA package(3), which performs Grand canonical global optimization (GCGO) samplings for the (111) facet of pure metals (Au and Ru) and alloys (variable Au:Ru ratio) with a

random amount of adsorbates and/or defects. The sampled configurations are then locally optimized by density functional theory calculations using the VASP program (version 6.4.1)(4, 5). The PBEsol functional(6) is adopted with PBE\_PAW pseudopotentials(5) and D3 correction(7) to balance the performance on both solid state and surface adsorption energetics. The convergence criteria for electronic and force minimization are  $10^{-5}$  eV and  $2.5 \times 10^{-2}$  eV/Å, respectively. The Brillouin zone is sampled using  $\Gamma$ -centered  $3 \times 3 \times 1$   $k$ -points, and the kinetic energy cutoff for the planewaves is 400 eV. The local optimization trajectories from GCGO sampling are filtered based on force magnitude and structural similarity. The curated dataset is then used to fine-tune the MACE-MP-0-medium foundation model(8) for 100 epochs. Dataset distribution and model performance are shown in Fig. S21-S22.

Using the trained MLIP, transition state searches for large-scale interfacial vacancy diffusion are performed via the nudged elastic band method(9). Grand canonical Monte Carlo (GCMC)(10) simulations, as implemented in GOCIA, are also performed with MLIP on a  $5 \times 5 \times 10$  supercell of the (111) facet of the alloy (Au:Ru=5:1). Each simulation starts from a randomized alloy configuration with 1 ML H on top surface, and the system is relaxed to a local minimum after every GCMC move (H insertion/deletion, site-swapping, rattling). The chemical potential of H is calculated by  $\mu_H = 1/2 [G(H_2, gas) + k_B T \ln(p/p^\circ)]$ .

## Data analysis

### EELS

Dual-EELS spectra containing simultaneously acquired low-loss and high-loss signals were processed using the HyperSpy library. The zero-loss peak (ZLP) position was determined on a per-pixel basis, and energy drift across the scan was corrected by aligning all spectra to a common ZLP reference. Following alignment, spectra were normalized by the integrated ZLP intensity to account for sample thickness and probe-current variations. The ZLP tail was removed from the low-loss spectra by fitting a power-law background over the 1.2–1.7 eV energy range and subtracting the fitted background.

Energy-filtered maps were generated by integrating ZLP-normalized spectra over selected energy-loss windows using channel-averaged intensities. Au-associated plasmon maps were constructed by integrating over 2.3–2.5 eV, corresponding to the Au surface plasmon resonance, while Ru-associated maps were generated over 9.5–11 eV, corresponding to the Ru bulk plasmon feature. For Fig. S10, spatial masks defining Au-rich and Ru-rich regions were derived from the corresponding energy-filtered maps by thresholding regions of enhanced spectral intensity relative to the local background, with vacuum and low-signal regions excluded based on ZLP-normalized low-loss intensity. These masks were applied consistently across energy windows to enable spatially correlated analysis of Au and Ru spectral features.

For linescan measurements, spectra were spatially binned by a factor of two along the scan direction (1.24 nm per pixel prior to binning) and binned in energy by a factor of three (0.01 eV per channel prior to binning). At each position along the linescan, spectra were averaged over the corresponding spatial bin prior to analysis. For visualization, intensity profiles were smoothed using a Savitzky–Golay filter (window length = 13 points, second-order polynomial). Linescan plots were generated by plotting the averaged, background-subtracted spectral intensity as a function of distance along the scan, with distances calculated from the calibrated probe step size.

#### 4D STEM

Pre-annealing 4D-STEM datasets were processed using the py4DSTEM library. (11) Detector calibration was performed using a polycrystalline Au film on carbon as a reference standard to determine detector pixel geometry and reciprocal-space calibration (pixel size = 0.0384 Å<sup>-1</sup>). The raw 4D-STEM datacube (256 × 256 probe positions, 192 × 192 detector pixels) was cleaned of hot pixels and spatially binned to 128 × 128 probe positions. Mean and maximum diffraction patterns were used to define virtual detector geometries, and circular bright-field and annular dark-field images were generated to guide selection of a vacuum region for probe reconstruction. The probe semi-angle and diffraction-center coordinates extracted from the vacuum probe were used to generate a matched kernel for Bragg disk detection. Bragg disks were identified across all probe positions using template matching with subpixel refinement, and automated crystal orientation mapping (ACOM)(2) was performed by matching experimentally detected Bragg disk configurations to simulated diffraction templates to generate spatially resolved orientation maps.

Post-annealing 4D-STEM datasets were analyzed to distinguish Au and Ru domains. Experimentally measured Bragg vector magnitudes were compared to theoretically expected reciprocal-lattice spacings for FCC Au and HCP Ru, calculated from known lattice parameters, enabling assignment of detected Bragg disks to Au- or Ru-like scattering families. Phase-resolved ACOM was performed by matching local Bragg disk configurations to simulated diffraction templates for each phase, generating spatially resolved maps encoding crystallographic orientation and phase identity. Quantitative phase fractions were obtained by tallying probe positions assigned to each phase. Phase-selective reciprocal-space masks and annular integrations were applied to Bragg vector maps to independently isolate Au- and Ru-associated scattering ranges.

#### X-EDS

X-EDS spectrum images were processed using the HyperSpy library to generate background-subtracted, spatially resolved elemental maps of AuRu nanoparticles. Following spatial and spectral rebinning, element-specific spectral models were constructed by defining the relevant Au and Ru X-ray emission lines (Au L $\alpha$ , Au M $\alpha$ , Ru L $\alpha$ , Ru K $\alpha$ ), with Mg K $\alpha$  and O K $\alpha$  lines included for particles supported on MgO. For each pixel, integrated peak intensities were obtained after local background subtraction, performed by estimating the background from pre-

and post-edge energy windows adjacent to each characteristic line and subtracting this contribution from the peak region. Background-subtracted elemental maps were generated for each line. To isolate the nanoparticle from the vacuum and ensure consistent spatial comparison, a binary particle mask was constructed by thresholding the combined background-subtracted Au and Ru signals and applied uniformly across all elemental channels. Masked elemental maps were combined to visualize and quantify the spatial segregation of Au-rich and Ru-rich regions.

#### *Nanocrystal drift alignment and image cropping*

Frame-to-frame drift in all HAADF-STEM image series was corrected by phase correlation in Fourier space. Images were rescaled and rebinned to a common pixel size, padded to minimize edge effects, and aligned using subpixel shifts extracted from the cross-correlation peak. Aligned images were cropped to a common region centered on the nanoparticle prior to analysis.

#### *Nanocrystal segmentation and size determination using Otsu thresholding*

Nanocrystal size was determined from drift-corrected HAADF-STEM images using global Otsu thresholding, in which the grayscale intensity histogram is partitioned at the threshold that maximizes the between-class variance between foreground and background intensity distributions. Binary masks were generated from the grayscale intensity histogram to segment the particle from the background. Particle area was calculated from the mask and converted to physical units using the calibrated pixel size, and an effective diameter was obtained assuming a circular projection. Size uncertainty was estimated by repeating the analysis using inclusive, moderate, and conservative threshold values.

#### *Tomography*

The tomographic reconstructions in this work used the open-source Python package *quantEM*. (12) Using implicit neural representations with a neural network as a model regularizer, we jointly optimize the volume and the relative orientations of each tilt image, allowing for the most accurate reconstruction possible. This framework also compensates for the large missing wedge, minimizing streaking along the missing wedge direction. We also perform background subtraction using Bernstein polynomial fitting and a coarse cross-correlation alignment prior to reconstruction. The reconstruction ran for 100 iterations, where the volume and alignment parameters were fully converged.

## Supporting Information

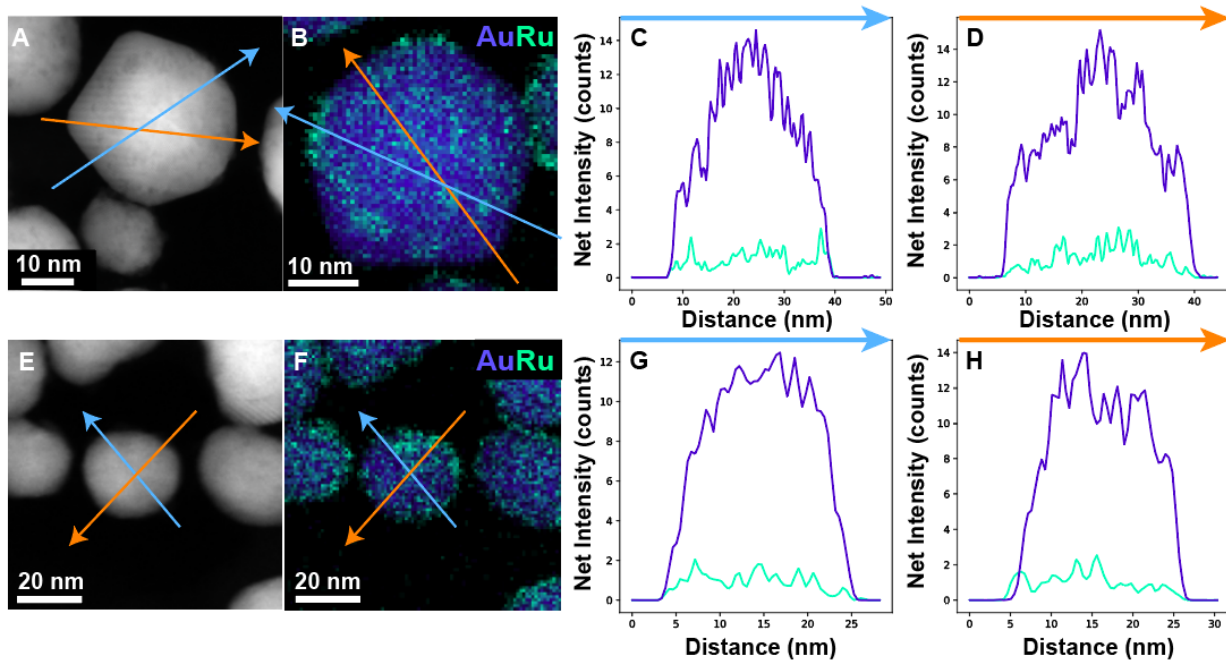


**Fig. S1. X-EDS analysis of Au–Ru intermixing pre-heating.** (A) HAADF-STEM image of an AuRu nanoparticle, 125° tilt relative to Fig. 1 in the main text, with line-scan paths indicated (blue and orange). (B) Corresponding X-EDS elemental map (reproduced from the main text) with line-scan locations marked. (C, D) X-EDS line profiles along the blue and orange paths, showing net intensities of the Au La and Ru K $\alpha$  lines, respectively. (E–H) Additional HAADF-STEM images, X-EDS maps, and corresponding line scans from different particles, confirming Au–Ru intermixing across the sample.

Z	Element	Family	Atomic Fraction (%)	Atomic Error (%)	Mass Fraction (%)	Mass Error (%)	Fit Error (%)
44	Ru	L	13.45	1.36	7.38	0.8	0.24
79	Au	L	86.55	1.36	92.62	0.8	0.04

**Table S1.** X-EDS quantification using the Brown-Powell ionization cross-section model of the entire X-EDS map shown in Fig. S1E.

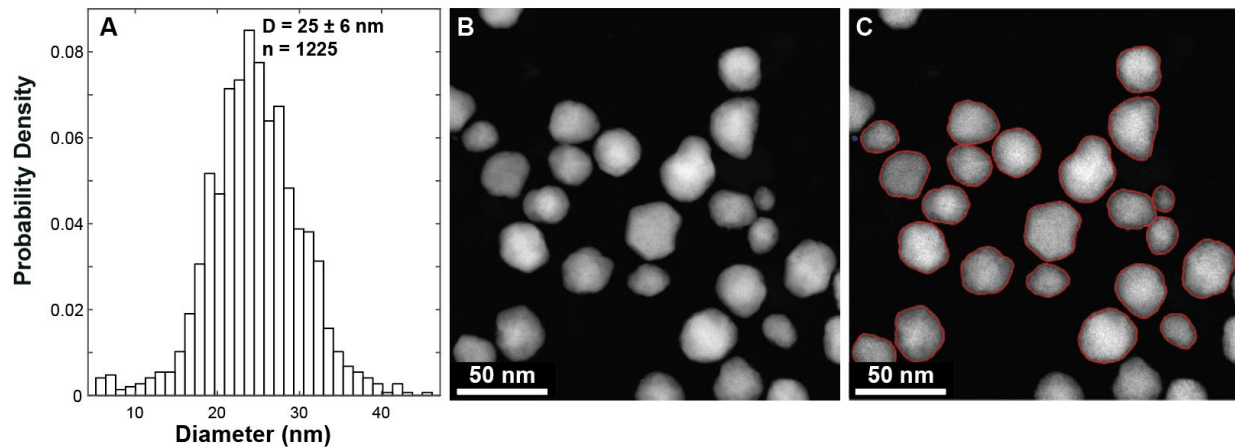


**Fig. S2. Native size distribution of AuRu nanocrystals.** (A) Diameter distribution of 1225 AuRu nanocrystals measured from HAADF-STEM images using the same analysis procedure as in (13). (B) Representative HAADF-STEM image used for particle sizing. (C) Corresponding thresholded image showing the particle boundary used to extract diameters.

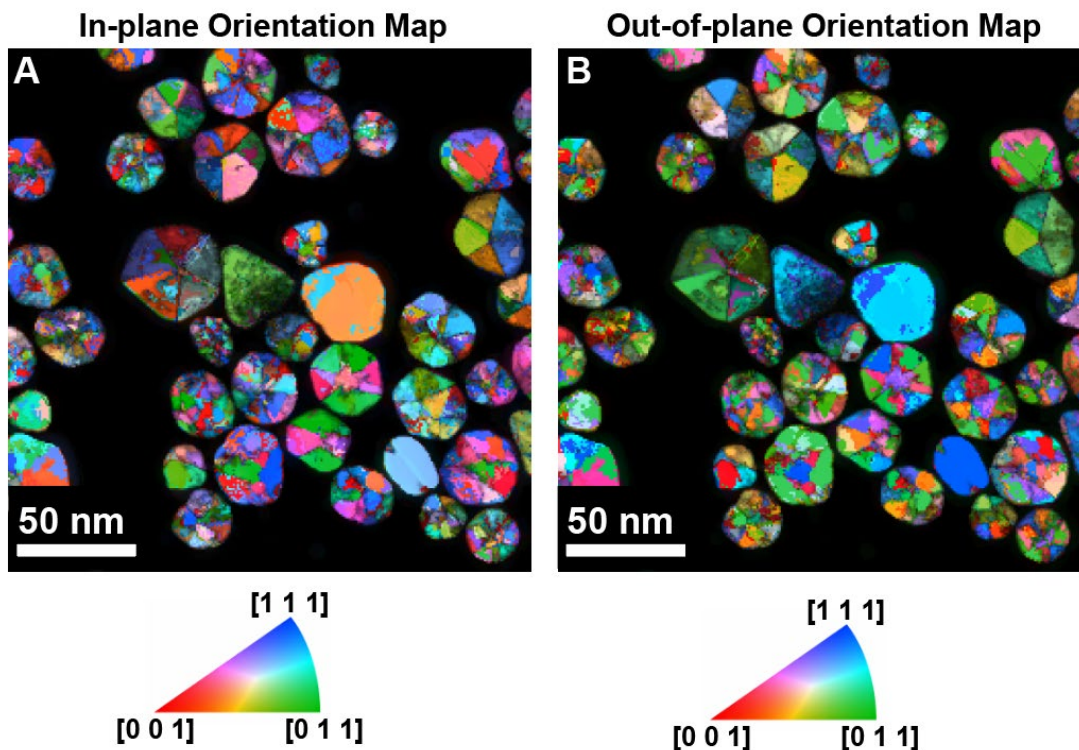


**Fig. S3. Orientation maps of AuRu nanocrystals derived from 4D-STEM.** (A) In-plane and (B) out-of-plane orientation maps showing the prevalence of pentatwinned particles and twin-boundary structure, with corresponding color bars indicating the principal crystallographic zone axes.

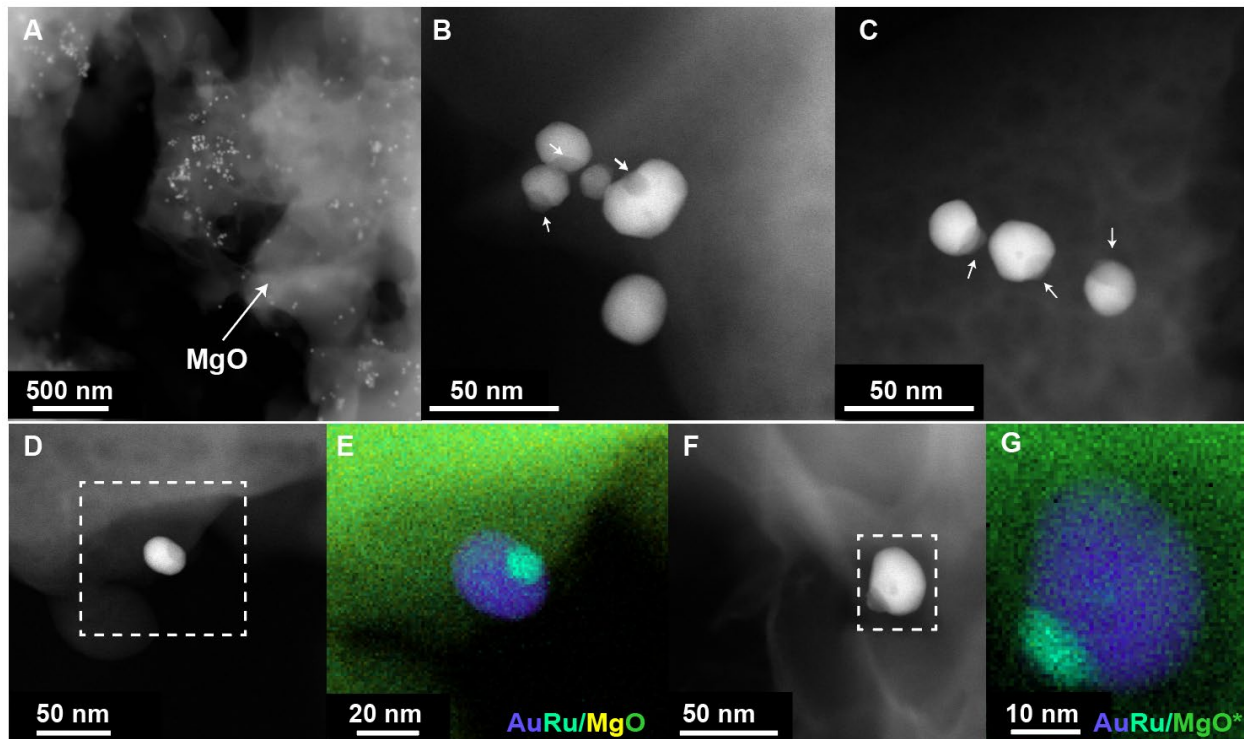


**Fig. S4. Vacuum annealing of AuRu nanocatalysts on MgO support induces phase segregation.** (A) HAADF-STEM image of AuRu nanocatalysts supported on MgO. (B, C) HAADF-STEM images of multiple supported particles after vacuum annealing, showing Au–Ru phase segregation identified by Z-contrast; white arrows mark Ru-rich regions. (D) HAADF-STEM image of a representative segregated AuRu nanocrystal on MgO. (E) Corresponding X-EDS elemental maps showing Au (La/M $\alpha$ ), Ru (K $\alpha$ /La), and Mg and O (K $\alpha$ ) raw signals. (F) HAADF-STEM image of an additional segregated AuRu nanocrystal on MgO. (G) X-EDS component map derived using non-negative matrix factorization (NMF), separating Au, Ru, and MgO\* regions. NMF was necessary due to the thickness of MgO in this region.

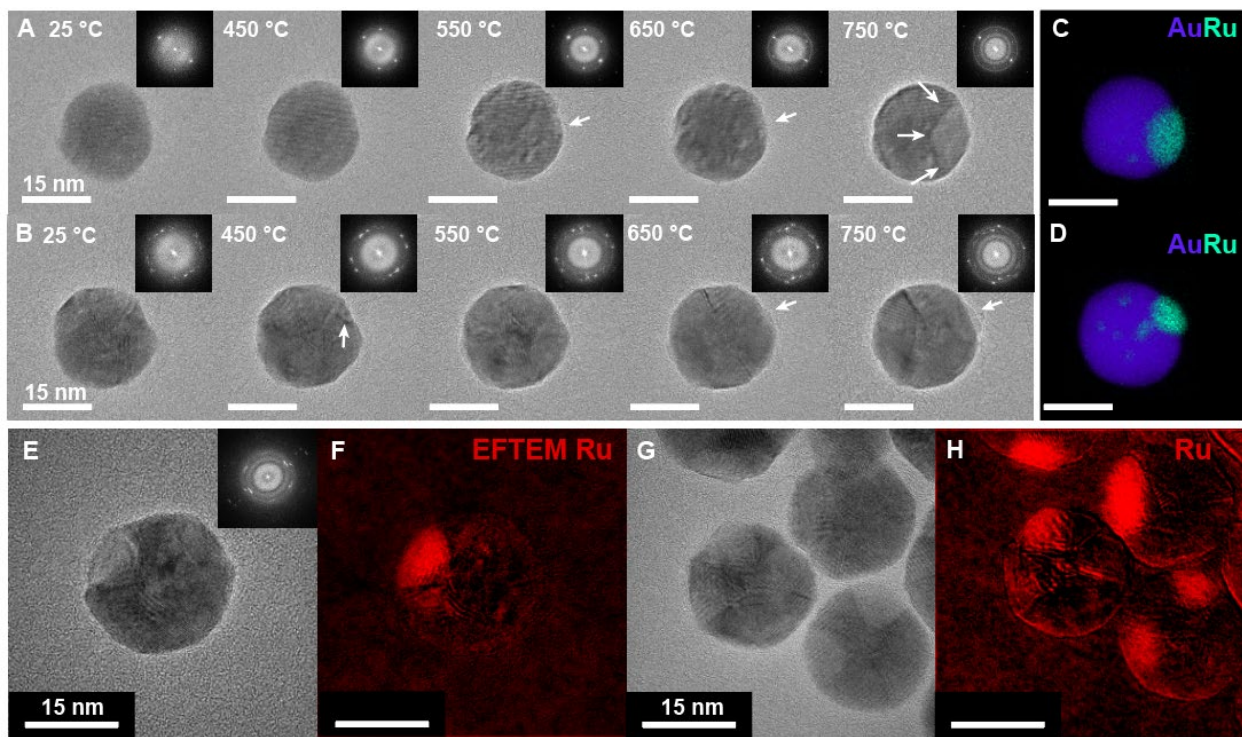


**Fig. S5. Additional statistics for vacuum-annealing-induced Au–Ru phase segregation.** (A, B) HRTEM image series with FFT insets of two representative AuRu nanocrystals during stepwise heating from room temperature to 750 °C at a ramp rate of 20 °C min<sup>-1</sup>, with 10-min holds at each temperature. Progressive Au–Ru phase segregation is indicated by the emergence of regions with distinct contrast. (C, D) Post-annealing STEM X-EDS elemental maps corresponding to the particles in (A, B), confirming spatial segregation of Au and Ru. (E) HRTEM image of an AuRu nanocrystal after vacuum annealing. (F) Corresponding EFTEM map of the Ru N<sub>2,3</sub> edge (red), highlighting Ru segregation. (G) HRTEM image of multiple AuRu nanocrystals following phase segregation. (H) Corresponding EFTEM Ru map for the particles shown in (G).

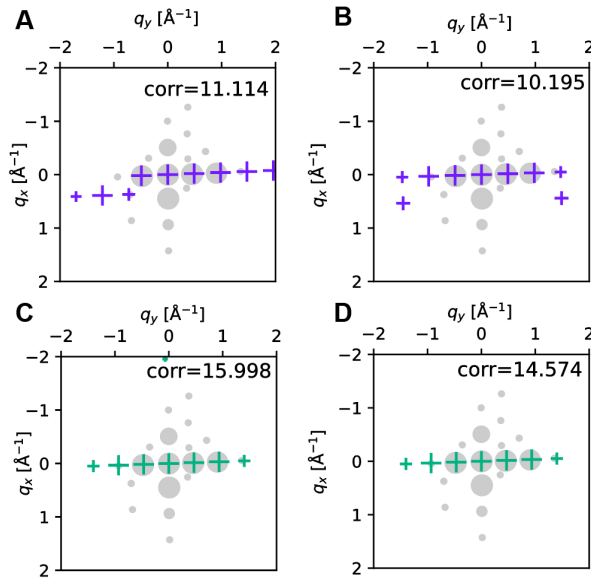


**Fig. S6. Phase assignment for the single-point diffraction pattern shown in Fig. 3E.**

(A, B) Best and second-best orientation matches assuming an Au FCC structure, with inset values indicating the corresponding correlation strengths. (C, D) Best and second-best orientation matches assuming a Ru HCP structure, with inset correlation strengths. The higher correlation strengths obtained for the Ru HCP assignments indicate that the diffraction pattern is best indexed as Ru.

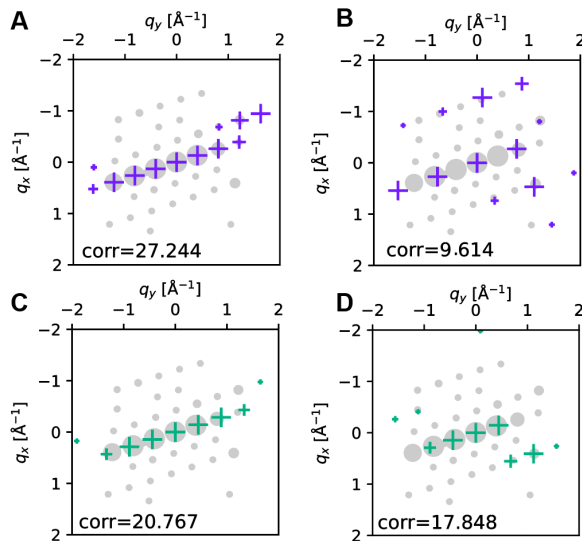


**Fig. S7. Phase assignment for the single-point diffraction pattern shown in Fig. 3F.**

(A, B) Best and second-best orientation matches assuming an Au FCC structure, with inset values indicating the corresponding correlation strengths. (C, D) Best and second-best orientation matches assuming a Ru HCP structure, with inset correlation strengths. The higher correlation strengths obtained for the Au FCC assignments indicate that the diffraction pattern is best indexed as Au.

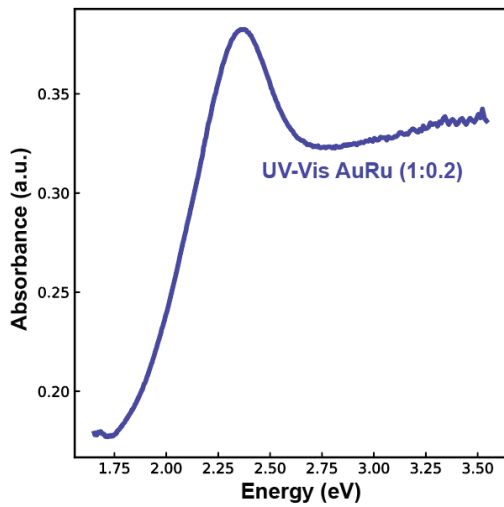


**Fig. S8.** UV–Vis absorbance spectra of AuRu (1:0.2) nanoparticles showing a surface plasmon resonance centered at ~2.4 eV, slightly red-shifted relative to the vacuum monochromated EELS resonance due to the aqueous environment.

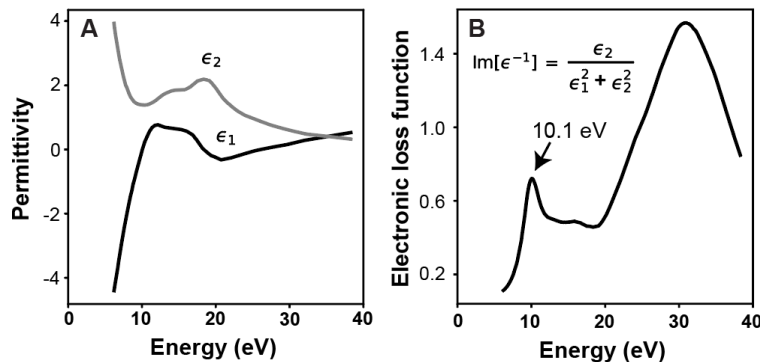


**Fig. S9.** Electronic loss function of Ru showing a bulk plasmon feature. (A) Bulk refractive index data digitized from the published measurements of Cox *et al.* and replotted(14). (B) Corresponding electronic loss function calculated from the refractive index data in (A), revealing a Ru bulk plasmon at 10.1 eV.

The weak loss feature at 10–11 eV is observed in low-loss EELS after phase segregation and is spatially confined to the Ru-rich domains (main text Fig. 3I, K, L). This spatial localization is inconsistent with an Au-origin loss mechanism: the dominant collective valence excitation of metallic Au is the bulk plasmon at 9.02 eV(15), which would be expected to be strongest in Au-rich regions and to scale with local Au thickness rather than anticorrelate with the Au plasmon map.

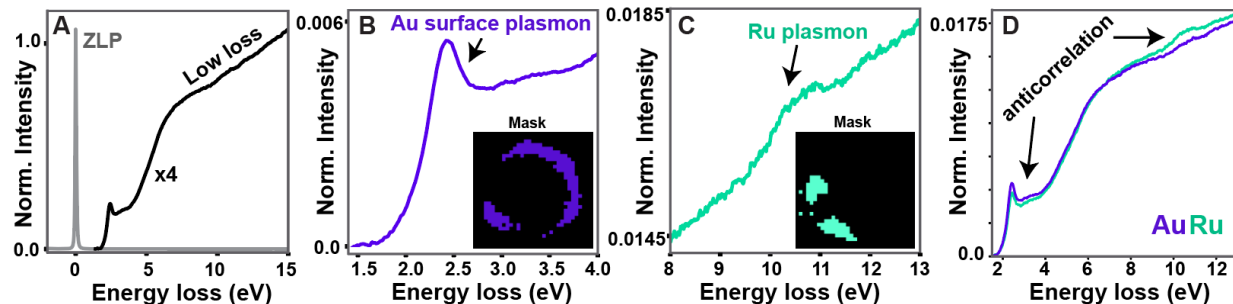


**Fig. S10. Low-loss EELS analysis of Au and Ru plasmon modes.** (A) Overlaid low-loss EELS spectra showing the zero-loss peak (ZLP) and plasmon features associated with Au and Ru. (B) Averaged Au surface plasmon spectrum near 2.5 eV, extracted from regions of high Au signal indicated by the mask in the inset. (C) Averaged Ru plasmon spectrum near 10 eV, extracted from regions of high Ru signal indicated by the mask in the inset. (D) Overlaid full low-loss spectra from the two masked regions, highlighting the anticorrelation between Au and Ru plasmon features.

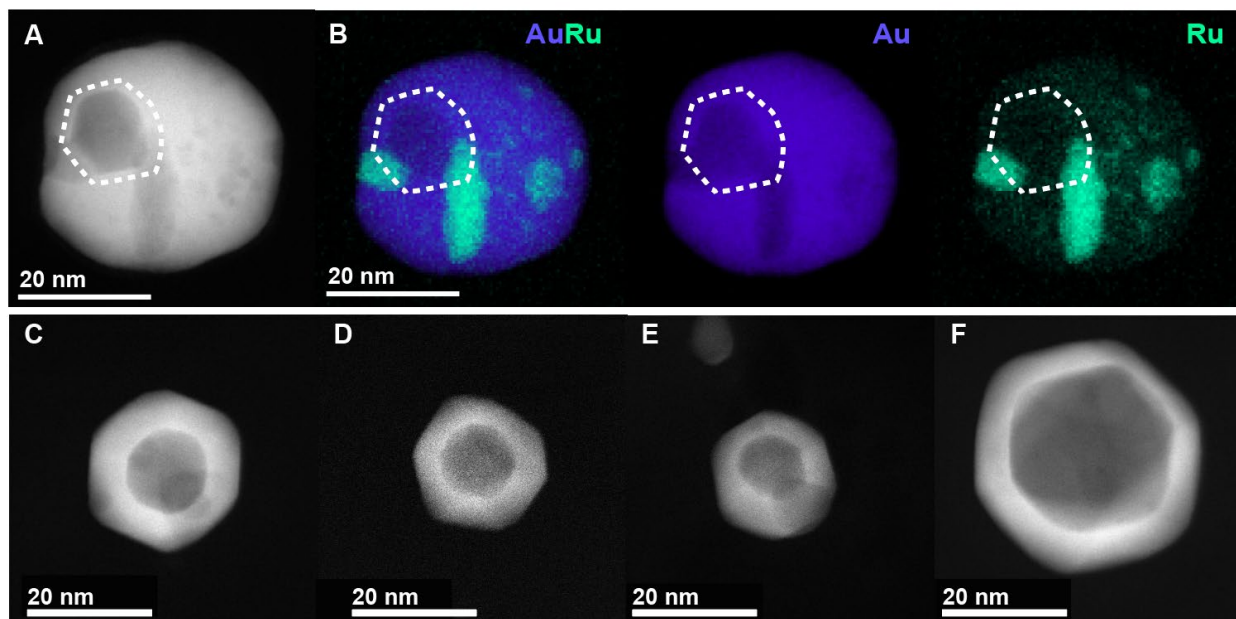


**Fig. S11. Additional statistics showing void formation in the presence of a H<sub>2</sub>:N<sub>2</sub> (3:1) gas mixture.** (A) HAADF-STEM image of an AuRu nanocrystal heated in a H<sub>2</sub>:N<sub>2</sub> (3:1) gas environment, showing a faceted internal void (dashed outline). (B) Corresponding X-EDS elemental maps (Au Ma/L $\alpha$  and Ru La/K $\alpha$ ), overlaid and separated by element, confirming the absence of signal within the void region. (C-F) HAADF-STEM images of AuRu nanocrystals subjected to extended O<sub>2</sub> plasma cleaning (3–5 min) and subsequently heated under 350 Torr H<sub>2</sub>:N<sub>2</sub> (3:1) gas. Observation of voids at lower pressure is directly attributed to increased O<sub>2</sub> plasma cleaning, introducing more vacancies and surface defect states for H-Ru binding and adsorption. Unless otherwise noted, all samples in this work were plasma cleaned for 60 s to minimize surface damage.

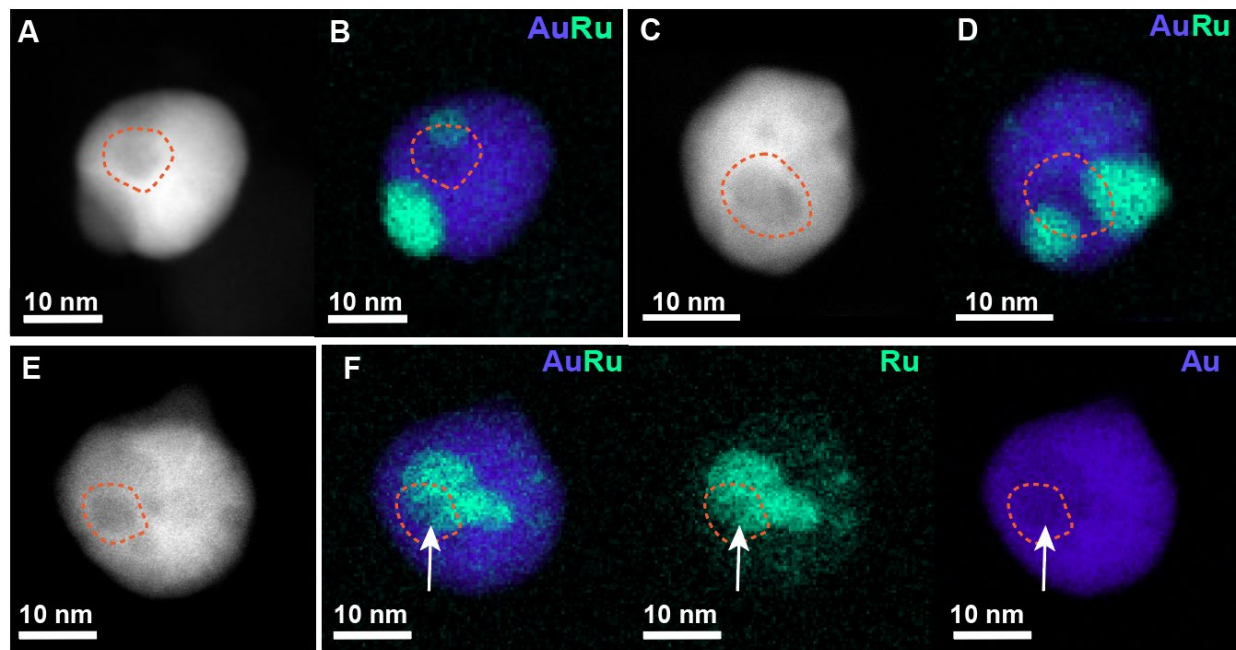


**Fig. S12. Nanovoid formation under pure H<sub>2</sub> at ~1 atm.** (A, C, E) HAADF-STEM images of representative AuRu nanocrystals annealed in pure H<sub>2</sub>, each exhibiting an internal nanovoid (dashed outlines in orange). (B, D, F) Corresponding X-EDS elemental maps of the particles in (A), (C), and (E), respectively. Overlaid Au and Ru maps, together with isolated elemental channels, confirm the diminished signal within the void regions and further reveal the spatial relationship between Ru-rich domains and nanovoid formation.

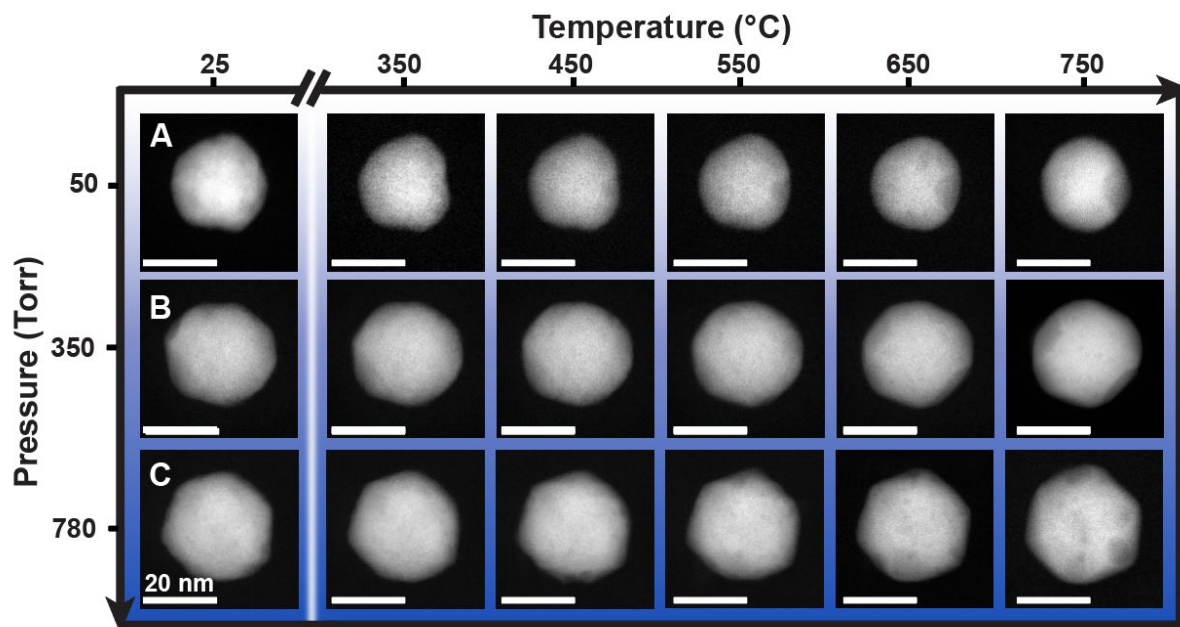


**Fig. S13. Additional statistics for the pressure-dependent restructuring of AuRu nanocatalysts in a 3:1 H<sub>2</sub>:N<sub>2</sub> atmosphere.** (A-C) *In situ* HAADF-STEM image sequences of representative AuRu nanocrystals during stepwise heating to 750 °C (100 °C increments) under increasing H<sub>2</sub>:N<sub>2</sub> (3:1) pressure. (A) At 50 Torr (0.07 atm), Au–Ru phase segregation resembles vacuum annealing (cf. Fig. 2A). (B) At 350 Torr (0.46 atm), segregation persists. (C) At 782 Torr (~1 atm), the particle maintains its hexagonal-type faceting, and multiple Ru regions can be observed.

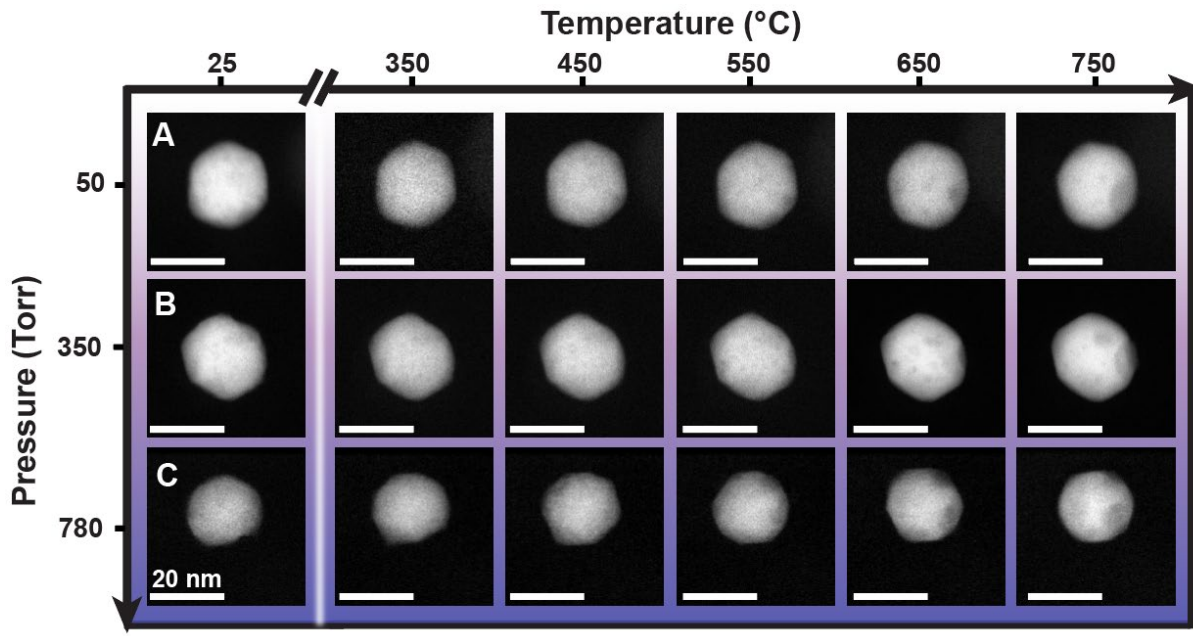


**Fig. S14. Additional statistics for the pressure-dependent restructuring of AuRu nanocatalysts in a 3:1 H<sub>2</sub>:N<sub>2</sub> atmosphere.** (A-C) *In situ* HAADF-STEM image sequences of representative AuRu nanocrystals during stepwise heating to 750 °C (100 °C increments) under increasing H<sub>2</sub>:N<sub>2</sub> (3:1) pressure. (A) At 50 Torr (0.07 atm), Au–Ru phase segregation resembles vacuum annealing (cf. Fig. 2A). (B) At 350 Torr (0.46 atm), segregation persists. (C) At 782 Torr (~1 atm), the particle moves towards a more hexagonal-type faceting around 450 °C, which is maintained towards higher temperatures.

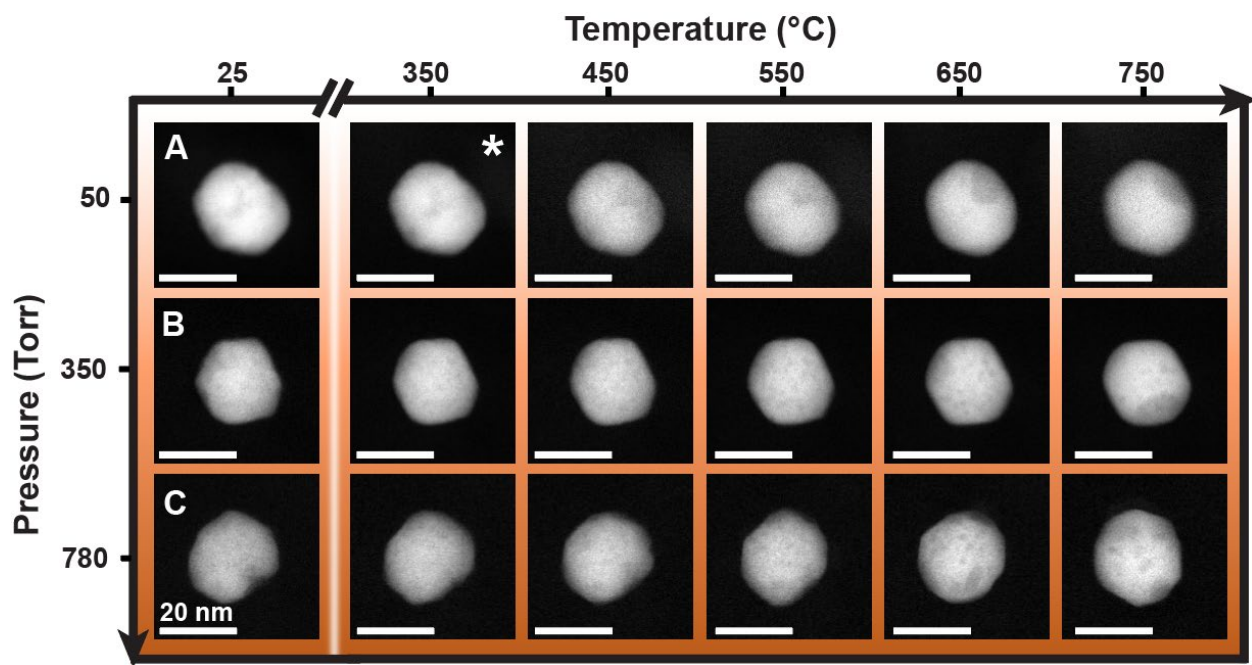


**Fig. S15. Additional statistics for the pressure-dependent restructuring of AuRu nanocatalysts in a 3:1 H<sub>2</sub>:N<sub>2</sub> atmosphere. (A-C) In situ HAADF-STEM image sequences of representative AuRu nanocrystals during stepwise heating to 750 °C (100 °C increments) under increasing H<sub>2</sub>:N<sub>2</sub> (3:1) pressure. (A) At 50 Torr (0.07 atm), Au–Ru phase segregation resembles vacuum annealing (cf. Fig. 2A). \*Imaging was performed at 150 °C; no image was collected at 350 °C during this heating sequence. (B) At 350 Torr (0.46 atm), segregation persists. (C) At 782 Torr (~1 atm), the particle morphology begins to evolve around 550 °C towards the more faceted final structure seen at 750 °C.**

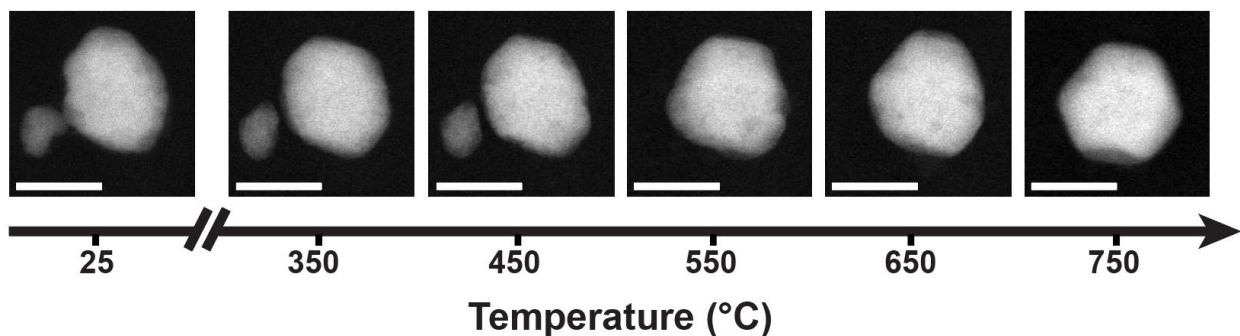


**Fig. S16. Facet evolution and particle coalescence in a 3:1 H<sub>2</sub>:N<sub>2</sub> atmosphere at 782 Torr. HAADF-STEM image series showing the coalescence of neighboring AuRu nanoparticles at 550 °C, followed by morphological evolution into a hexagonally faceted particle with a segregated Ru-rich region**

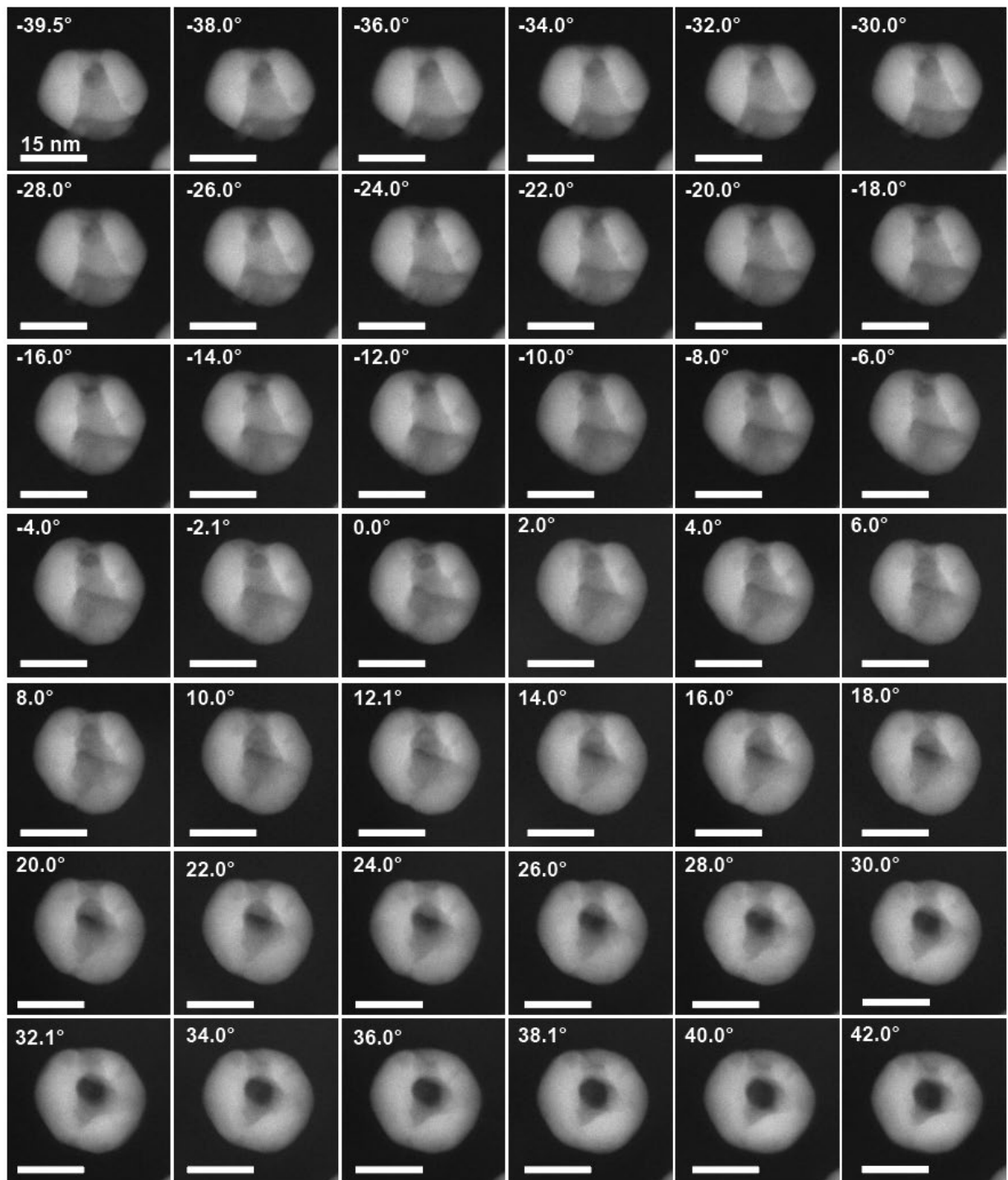


**Fig.S17. Experimental tomographic tilt series of the AuRu nanocrystal post-exposure to H<sub>2</sub>:N<sub>2</sub> (3:1) gas at 782 Torr.** 42 HAADF-STEM images of the nanocatalyst with a tilt range from -39.5° to +42.0°. Scale bar, 15 nm.

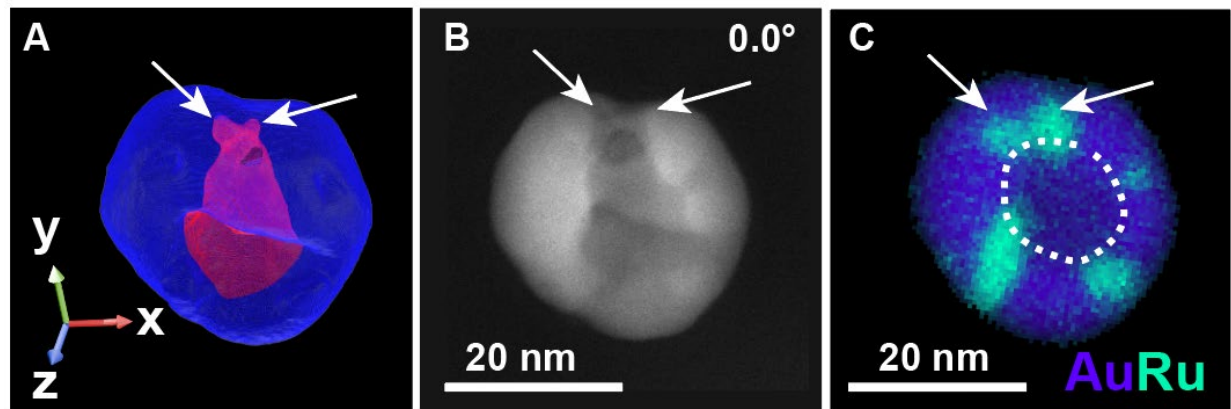


**Fig.S18. Cross-correlation of tomography, HAADF-STEM, and X-EDS showing the presence of a Ru channel.** (A) Machine-learning-assisted tomographic reconstruction shown as isosurfaces at thresholds of 1.2 (red) and 2.2 (blue), highlighting the internal cavity morphology. (B) HAADF-STEM image from the tilt series at 0.0°. (C) Corresponding X-EDS elemental map reproduced from Fig. 4 (main text), with arrows indicating the mid-particle Ru-rich channel intersecting the void.

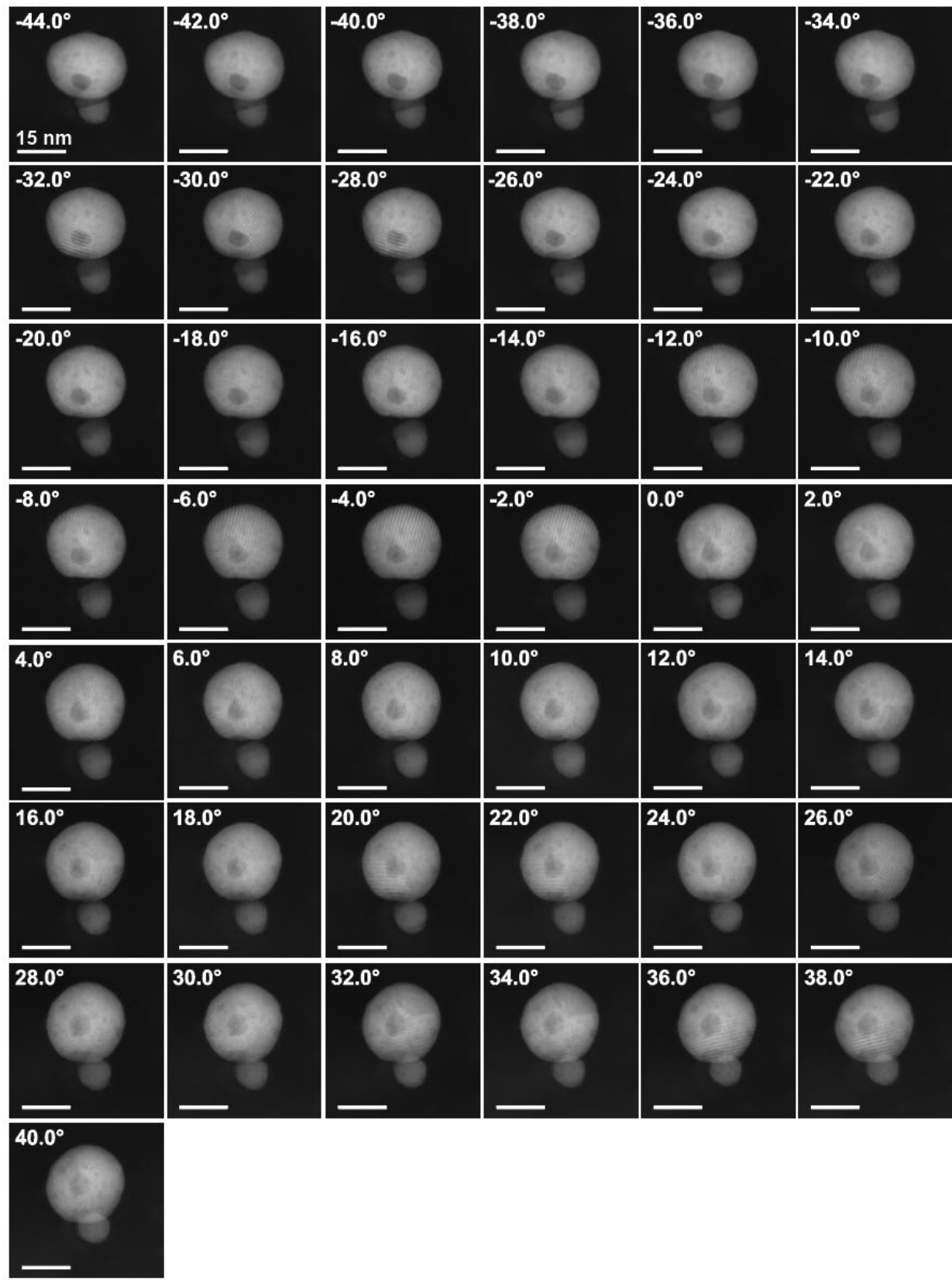


**Fig. S19. Experimental tomographic tilt series of the AuRu nanocrystal post-exposure to pure H<sub>2</sub> gas at 760 Torr.** 43 HAADF-STEM images of the nanocatalyst with a tilt range from -44.0° to +40.0°. Scale bar, 15 nm.

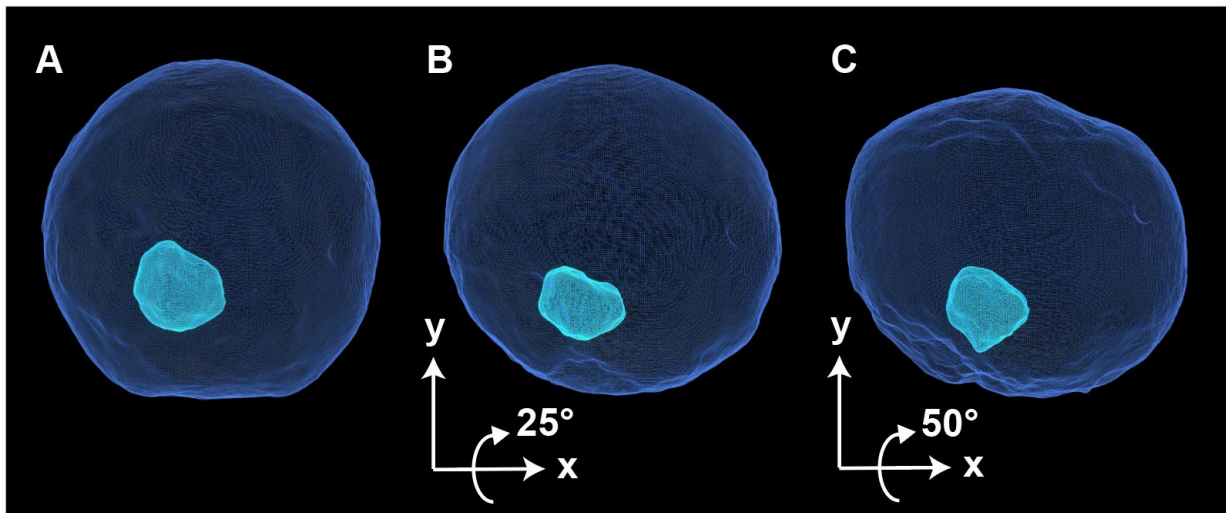


**Fig. S20. Machine-learning-assisted tomographic reconstruction from multiple viewing directions revealing the 3D geometry of the internal nanovoid.** Isosurface at 1.05 converted to wire mesh, with particle exterior (blue) and internal void (cyan). (A) Face-one view matching the 0.0° tilt from Figure S15. (B) View with 25° tilt along the x-axis. (C) View with a 50° tilt along the x-axis.

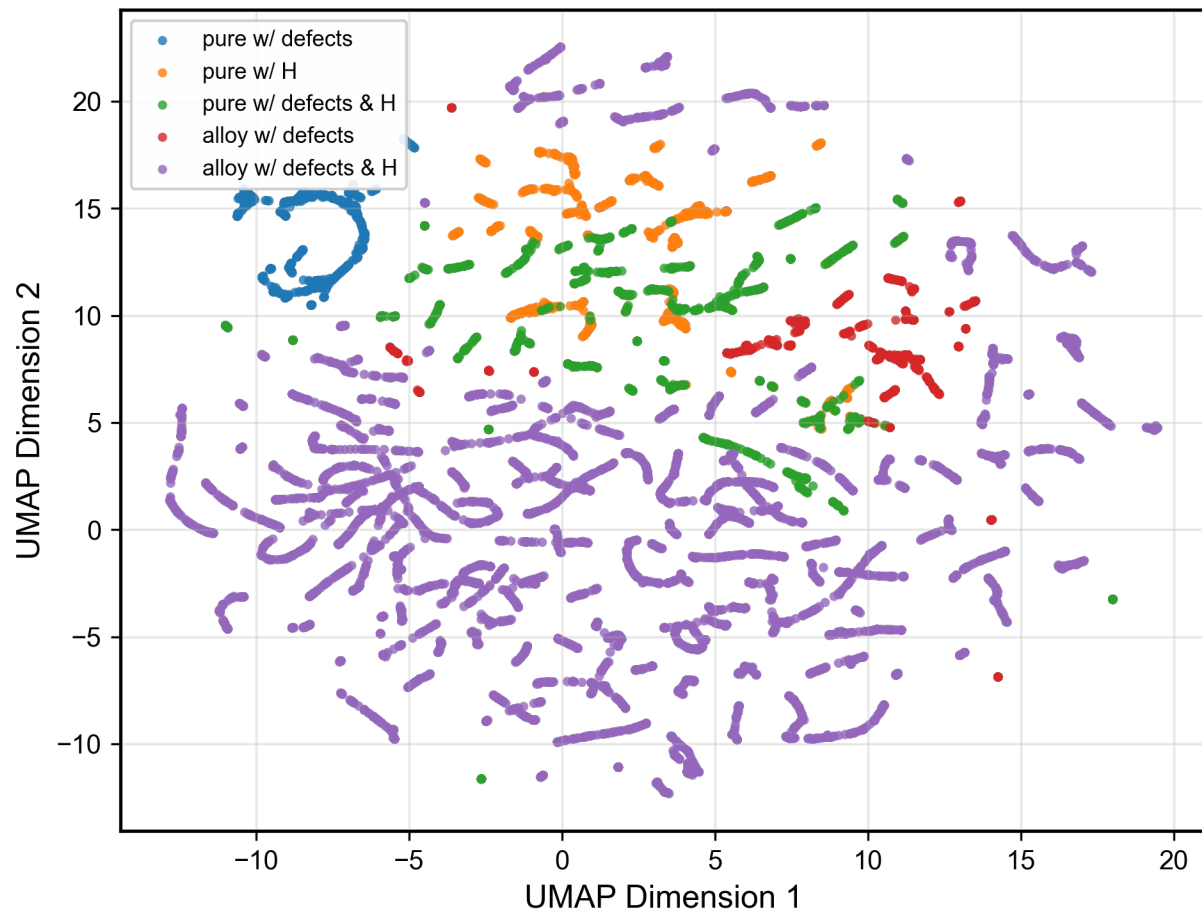


**Fig. S21. Visualization of the training dataset distribution.** UMAP projection of 15,695 structures from five sampling groups (pure/alloy systems with/without defects and/or H). Structures were characterized using SOAP descriptors, reduced via Incremental PCA (50 components), and projected to 2D space using UMAP. Each point represents a sampled configuration, colored by its corresponding group.

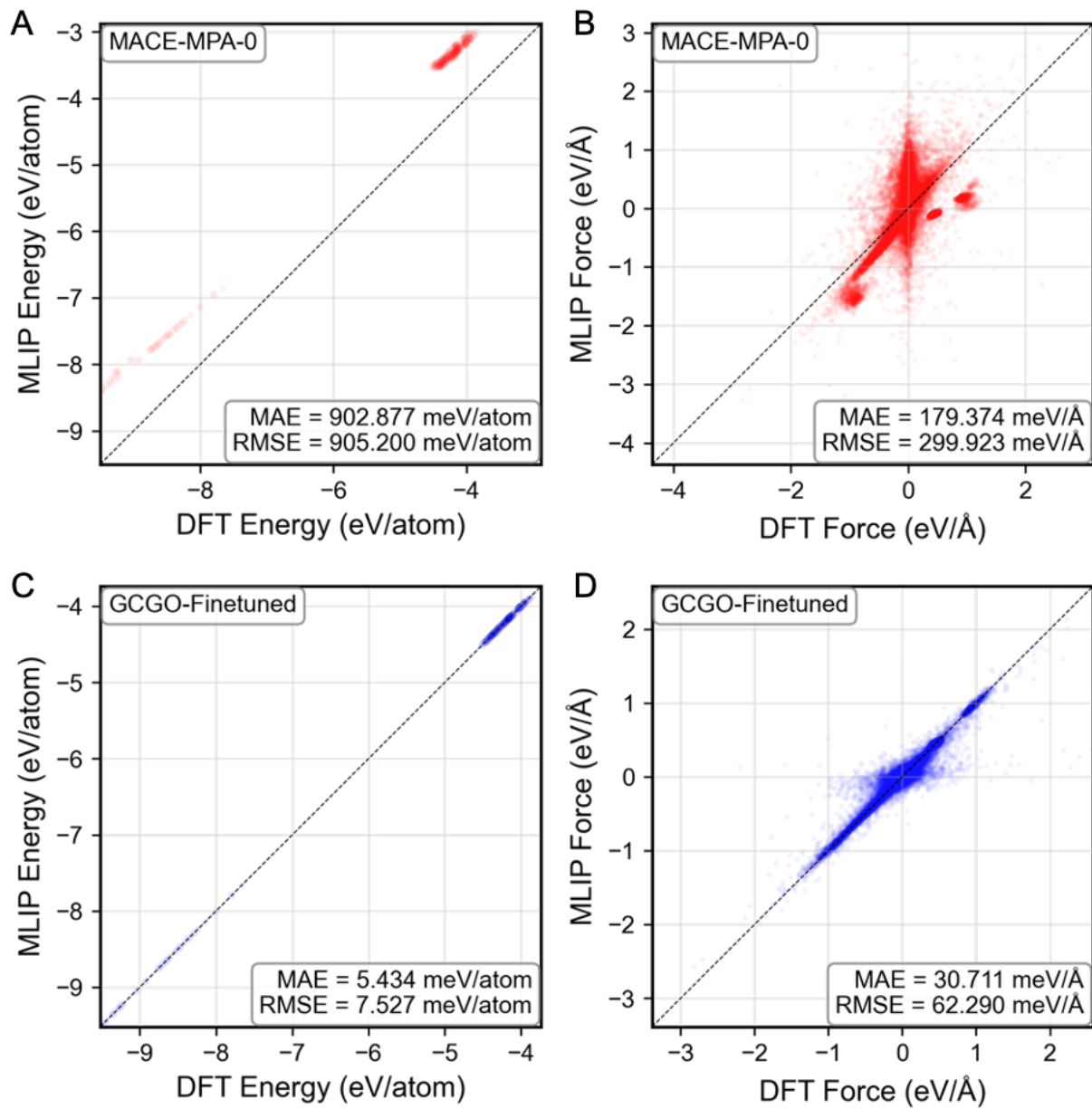


**Fig. S22. Performances of the MLIP on the test dataset.** Parity plots for (A) energy and (B) force of the MACE-MPA-0 foundation model, and for (C) energy and (D) force of our fine-tuned version on GCGO samples. Each semi-transparent marker represents a data point.

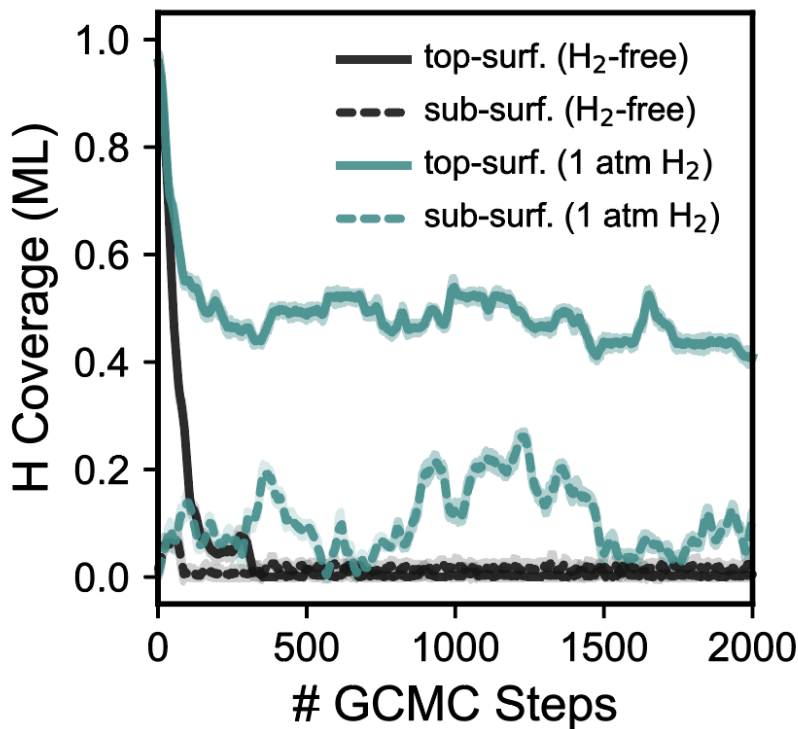


**Fig. S23. H-coverage in H<sub>2</sub>-free and 1 atm H<sub>2</sub> conditions.** In H<sub>2</sub>-free conditions (black), H coverage converges to 0. In 1 atm H<sub>2</sub> conditions (green), we see the formation of ~0.5 ML of H atoms on the Ru surface and the presence of some subsurface H.

## References:

1. L. Yuan, B. B. Bourgeois, E. Begin, Y. Zhang, A. X. Dai, Z. Cheng, A. S. McKeown-Green, Z. Xue, Y. Cui, K. Xu, Y. Wang, M. R. Jones, Y. Cui, A. Majumdar, J. L. Bao, J. A. Dionne, Atmospheric pressure ammonia synthesis on AuRu catalysts enabled by plasmon-controlled hydrogenation and nitrogen-species desorption, *arXiv [physics.chem-ph]* (2024). <http://arxiv.org/abs/2410.01300>.
2. C. Ophus, S. E. Zeltmann, A. Bruefach, A. Rakowski, B. H. Savitzky, A. M. Minor, M. C. Scott, Automated crystal orientation mapping in py4DSTEM using sparse correlation matching. *Microsc. Microanal.* **28**, 1–14 (2022).
3. Z. Zhang, W. Gee, R. H. Lavroff, A. N. Alexandrova, GOCIA: a grand canonical global optimizer for clusters, interfaces, and adsorbates. *Phys. Chem. Chem. Phys.* **27**, 696–706 (2025).
4. G. Kresse, J. Furthmüller, Efficient iterative schemes for ab initio total-energy calculations using a plane-wave basis set. *Phys. Rev. B Condens. Matter* **54**, 11169–11186 (1996).
5. G. Kresse, D. Joubert, From ultrasoft pseudopotentials to the projector augmented-wave method. *Phys. Rev. B Condens. Matter* **59**, 1758–1775 (1999).

6. J. P. Perdew, A. Ruzsinszky, G. I. Csonka, O. A. Vydrov, G. E. Scuseria, L. A. Constantin, X. Zhou, K. Burke, Restoring the density-gradient expansion for exchange in solids and surfaces. *Phys. Rev. Lett.* **100**, 136406 (2008).

7. S. Grimme, J. Antony, S. Ehrlich, H. Krieg, A consistent and accurate ab initio parametrization of density functional dispersion correction (DFT-D) for the 94 elements H-Pu. *J. Chem. Phys.* **132**, 154104 (2010).

8. I. Batatia, P. Benner, Y. Chiang, A. M. Elena, D. P. Kovács, J. Riebesell, X. R. Advincula, M. Asta, M. Avaylon, W. J. Baldwin, F. Berger, N. Bernstein, A. Bhowmik, F. Bigi, S. M. Blau, V. Cárare, M. Ceriotti, S. Chong, J. P. Darby, S. De, F. Della Pia, V. L. Deringer, R. Elijošius, Z. El-Machachi, E. Fako, F. Falcioni, A. C. Ferrari, J. L. A. Gardner, M. J. Gawkowski, A. Genreith-Schriever, J. George, R. E. A. Goodall, J. Grandel, C. P. Grey, P. Grigorev, S. Han, W. Handley, H. H. Heenen, K. Hermansson, C. H. Ho, S. Hofmann, C. Holm, J. Jaafar, K. S. Jakob, H. Jung, V. Kapil, A. D. Kaplan, N. Karimitari, J. R. Kermode, P. Kourtis, N. Kroupa, J. Kullgren, M. C. Kuner, D. Kuryla, G. Liepuoniute, C. Lin, J. T. Margraf, I.-B. Magdău, A. Michaelides, J. H. Moore, A. A. Naik, S. P. Niblett, S. W. Norwood, N. O'Neill, C. Ortner, K. A. Persson, K. Reuter, A. S. Rosen, L. A. M. Rosset, L. L. Schaaf, C. Schran, B. X. Shi, E. Sivonxay, T. K. Stenczel, C. Sutton, V. Svahn, T. D. Swinburne, J. Tilly, C. van der Oord, S. Vargas, E. Varga-Umbrich, T. Vegge, M. Vondrák, Y. Wang, W. C. Witt, T. Wolf, F. Zills, G. Csányi, A foundation model for atomistic materials chemistry. *J. Chem. Phys.* **163** (2025).

9. G. Mills, H. Jónsson, G. K. Schenter, Reversible work transition state theory: application to dissociative adsorption of hydrogen. *Surf. Sci.* **324**, 305–337 (1995).

10. R. B. Wexler, T. Qiu, A. M. Rappe, Automatic prediction of surface phase diagrams using ab initio grand canonical Monte Carlo. *J. Phys. Chem. C Nanomater. Interfaces* **123**, 2321–2328 (2019).

11. B. H. Savitzky, S. E. Zeltmann, L. A. Hughes, H. G. Brown, S. Zhao, P. M. Pelz, T. C. Pekin, E. S. Barnard, J. Donohue, L. Rangel DaCosta, E. Kennedy, Y. Xie, M. T. Janish, M. M. Schneider, P. Herring, C. Gopal, A. Anapolsky, R. Dhall, K. C. Bustillo, P. Ercius, M. C. Scott, J. Ciston, A. M. Minor, C. Ophus, Py4DSTEM: A software package for four-dimensional scanning transmission electron microscopy data analysis. *Microsc. Microanal.* **27**, 712–743 (2021).

12. C. Lim, C. Casert, A. R. C. McCray, S. Lee, A. Barnum, J. Dionne, C. Ophus, Missing wedge inpainting and joint alignment in electron tomography through implicit neural representations, *arXiv [eess.IV]* (2025). <https://doi.org/10.48550/arXiv.2512.08113>.

13. A. S. McKeown-Green, J. C. Ondry, M. F. Crook, J. J. Calvin, A. P. Alivisatos, Examining the role of chloride ligands on defect removal in imperfectly attached semiconductor nanocrystals for 1D and 2D attachment cases. *J. Phys. Chem. C Nanomater. Interfaces* **127**, 7740–7751 (2023).

14. J. T. Cox, G. Hass, J. B. Ramsey, W. R. Hunter, Reflectance and optical constants of evaporated ruthenium in the vacuum ultraviolet from 300 to 2000 Å. *J. Opt. Soc. Am.* **64**, 423 (1974).

15. S. Tehuacanero-Cuapa, J. Reyes-Gasga, A. Rodríguez-Gómez, D. Bahena, I. Hernández-Calderón, R. García-García, The low-loss EELS spectra from radiation damaged gold nanoparticles. *J. Appl. Phys.* **120**, 164302 (2016).